# UNIVERSITÉ DE STRASBOURG

*ÉCOLE DOCTORALE DES SCIENCES CHIMIQUES*

**ISIS (UMR 7006) et IPCMS (UMR 7504)**

# THÈSE

présentée par :

**Adriano ANGELONE**

soutenue le : **19 Septembre 2017**

pour obtenir le grade de : **Docteur de l'Université de Strasbourg**

Discipline/ Spécialité : **Physique**

## Strongly Correlated Systems of Bosons and Fermions: a Diagrammatic, Variational and Path Integral Monte Carlo study

**THÈSE dirigée par :**

| | |
|---|---|
| **Prof. PUPILLO Guido** | Professeur, Université de Strasbourg |

**RAPPORTEURS :**

| | |
|---|---|
| **Prof. POLLET Lode** | Professeur, Ludwig-Maximilians-Universität München |
| **Prof. VIGNOLO Patrizia** | Professeur, Institut Non-Linéaire de Nice |

---

**AUTRES MEMBRES DU JURY :**

| | |
|---|---|
| **Dr. MORONI Saverio** | Directeur de Recherche, DEMOCRITOS National Simulation Center |
| **Prof. PUPILLO Guido** | Professeur, Université de Strasbourg |

## Acknowledgements

First and foremost, I would like to thank my advisor, Prof. Guido Pupillo, for the many things I learned from him, about physics and more.

A heartfelt thanks goes to Dr. Fabio Mezzacapo, whom I have been honored to have as a mentor and friend, for helping me both in the bright and the dark moments.

My gratitude goes to my colleagues, and in particular to Guido Masella, Dr. Luca Lepori, Dr. Davide Vodola, Dr. Edoardo Tignone, Dr. David Hagenmuller, and Thomas Botzung, for their help and assistance during these years.

I would also like to thank Prof. Nikolay Prokof'ev for his illuminating advice and patient assistance.

Finally, I would like to thank my mother, for her continuous support.

# Contents

# List of Figures

# Chapter 1

# Introduction

## 1.1 Outline of the Work

*This section contains a brief outline of the thesis, describing the focus of my studies and the structure of my work.*

In recent years, the great progress achieved in the field of cold atom experiments has drawn closer the domains of Atomic and Condensed Matter physics. The link between these two domains is given by the concept of quantum simulation, i.e. the creation of an experiment which implements a Hamiltonian of interest (such as, e.g., a candidate model for an unexplained phenomenon) in a clean and controllable fashion.

The perspective of quantum simulation has increased the interest in the study of strongly correlated Hamiltonians, which was already of considerable importance due to the connection between the latter and some of the most intriguing scenarios in Condensed Matter physics (such as, e.g., high-$T_c$ superconductivity). Due to the complexity of strongly correlated problems, numerical techniques usually offer the most reliable approach to treat them.

The focus of my thesis is the investigation, via state-of-the-art nu-

merical approaches, of strongly correlated models of bosons and fermions, of interest for Atomic and Condensed Matter physics.

I study bosonic lattice Hamiltonians with extended-range interactions. I perform my investigations via Path Integral Monte Carlo simulations with Worm Updates, using an implementation of the algorithm written by myself. My main result is the demonstration of a superglass (i.e., a disordered supersolid) in the absence of frustration sources in the system, usually employed to generate glassy physics. These phases should be of direct relevance for experimental realizations with cold Rydberg-dressed atoms.

I also study the fermionic $t - J$ model in the presence of two mobile holes via the Variational Monte Carlo approach with the Entangled Plaquette States Ansatz. My study is foundational to the extension of this approach in order to study other fermionic problems of considerable interest, where the physical picture is still under debate (such as, e.g., the $t - J$ model in the case of finite hole concentration).

Finally, I discuss my work on Diagrammatic Monte Carlo, a recently introduced technique for the study of strongly correlated fermionic systems. I illustrate the approach and offer details about my implementation of this algorithm, motivating the chosen strategies and discussing possible future developments.

The remainder of the thesis is organized as follows. In section 1.2 and 1.3 I offer a quick overview of strongly correlated systems and cold atom experiments, respectively. In section 1.4 I give a brief outline of my results. The numerical techniques used to obtain the latter are introduced in chapter 2, and an in-depth discussion of my findings is offered in chapter 3. I offer in chapter 4 details about the Diagrammatic Monte Carlo method and discuss the state and possible future developments of my implementation of the approach. Finally, I draw the conclusions of my thesis in chapter 5.

The results exposed in section 3.1 can be found in

A. Angelone, F. Mezzacapo, and G. Pupillo,
*Superglass Phase of Interaction-Blockaded Gases on a Triangular Lattice*,
Phys. Rev. Lett. **116**, 135303 (2016)

T. Ying, M. Dalmonte, A. Angelone, F. Mezzacapo, P. Zoller and G. Pupillo,
*Cluster Bose Metals*,
arXiv:1606.04267 (2016)

The results discussed in section 3.2 can be found in

F. Mezzacapo, A. Angelone and G. Pupillo,
*Two holes in a two-dimensional quantum antiferromagnet: A variational study based on entangled-plaquette states*,
Phys. Rev. B **94**, 155120 (2016)

## 1.2 Strongly Correlated Systems

*This section contains a quick introduction to strongly correlated systems. I briefly illustrate some examples of many-body phenomena occurring in bosonic and fermionic systems, and describe the related research directions followed in the thesis.*

Physical systems known as *strongly correlated* (i.e., in which the behaviour of the degrees of freedom cannot be described effectively in terms of noninteracting entities) offer the possibility to observe some of the most interesting scenarios in Condensed Matter Physics. In particular, the latter include several examples of *Macroscopic Quantum Phenomena* (MQP), i.e. large-scale manifestation of the quantum nature of the system components.

A prominent example of MQP observed in bosonic systems is *superfluidity*, i.e. the property of a material sustaining persistent and dissipation-free flow. Superfluid behavior was first observed in $^4\mathrm{He}$, in which a second-order phase transition between a normal liquid phase and a superfluid state occurs at a critical temperature $T_\lambda \simeq 2.17$ K [1, 2]. A well-established theoretical framework for the physics of superfluids exists nowadays (see, e.g., [3], sec. A2 and references therein), and experimental observations of superfluidity have been reported in systems other than $^4\mathrm{He}$, such as cold atoms (see, e.g., [4]).

Superfluid phenomena also appears in *supersolids* (see for instance [3] and references therein), i.e. phases in which a crystalline structure coexists with superflow. The theoretical possibility of a supersolid phase in solid $^4\mathrm{He}$ was first considered decades ago, and different mechanisms for its appearance were proposed (see, e.g., [3], sec. A3 and references therein). The most relevant among these is the Andreev-Chester-Lifshitz scenario [5, 6], which explains supersolidity as the effect of the presence, with respect to a commensurate crystal, of defects such as vacancies or excess particles which can delocalize, giving rise to superfluidity. Despite early reports of experimental observation of

this phenomenon in solid $^4\mathrm{He}$ [7, 8], its possibility was ruled out by subsequent numerical [9, 10] and experimental [11] studies. Numerical simulations have however proven the existence of supersolid phases in several bosonic systems, ranging from lattice Hamiltonians (e.g. [12]) to free-space models with extended-range interactions (e.g. [13]).

The theoretical search of supersolid phases in systems of experimental interest is therefore an active field of research, as well as the investigation for phases which (like supersolids) show coexistence of different order parameters. My studies in this direction [14] will be briefly introduced in section 1.4.1 and thoroughly discussed in section 3.1.

Another example of MQP, observed in fermionic systems, is *superconductivity*, i.e. the loss of electric resistance and the appearance of anomalous magnetic behaviors which may be observed below a *critical temperature* $T_c$ in some materials.

In many of these, known as *conventional superconductors*, the properties of the superconducting state are described very well by the *Bardeen-Cooper-Schrieffer (BCS) theory* [15], which identifies electronic pairing as the key mechanism behind superconductivity.

Despite its successes, the BCS theory cannot reproduce the features of the superconducting behavior observed in some materials (for reviews on this topic see, e.g., [16, 17, 18]). As an example, superconducting behavior has been observed at temperatures of up to $\sim 130$ K, against a maximum theoretical prediction of the order of $30$ K within the BCS framework.

Materials showing these anomalous features are known as *high-$T_c$ superconductors*, and it is believed that their physics can be modeled by strongly correlated electronic Hamiltonians: candidates include the two-dimensional (2D) Hubbard and the so-called $t-J$ models [19]. The former is the simplest model for interacting electrons on a lattice, comprising only a uniform, nearest-neighbor hopping term and an on-site interaction between electrons of opposite spins. A strong-coupling expansion of the Hubbard model yields the $t-J$ Hamiltonian, which is

studied as an independent model on its own right due to its capability to reproduce some features of a particular class of high-$T_c$ superconductors, known as *cuprates*. For instance, the model reproduces the antiferromagnetic ground state observed in the cuprate phase diagram at zero doping.

Nevertheless, the relation between effective models such as the Hubbard or $t-J$ and the physics of high-$T_c$ superconductors is still not well established. One of the reasons for this lack of understanding is the fact that the aforementioned models do not generally admit exact analytical treatment, and most commonly used approximated analytical approaches (such as, e.g., mean field) fail to treat them, as well as many numerical methods.

As an example, exact diagonalization studies offer useful insight on the physics of the system, but are limited to relatively small system sizes (of the order of 30 sites for a spin system). This usually does not allow to obtain results which reliably approximate the thermodynamic limit. Similarly, *Path Integral Quantum Monte Carlo* (PIMC), one of the most important numerical methods in 2D, cannot be applied to simulate models like the Hubbard or $t-J$ at large sizes and low temperatures due to numerical instabilities arising from the fermionic nature of the Hamiltonian, collectively known as *sign problem* [20].

Given the aforementioned analytical and numerical difficulties in the study of strongly correlated fermionic systems, the investigation of the latter, as well as the development of new tools and methods to this end, is an important avenue of research. My studies in this direction [21] will be briefly introduced in section 1.4.2 and thoroughly discussed in section 3.2. Furthermore, in chapter 4 I will introduce a recently developed numerical technique for the study of strongly correlated fermionic systems, known as *Diagrammatic Monte Carlo* (DMC) (see, e.g., [22]). I will also discuss my implementation of the method, motivating the chosen strategies and illustrating possible future developments.

In recent years, interest in strongly correlated models has renewed due to the great progress achieved in the field of *quantum simulation* (see, e.g., [23, 24]). The idea behind this approach, first introduced in [25], is to study a Hamiltonian of interest (which may, for instance, be proposed to model a phenomenon of unknown origin) by implementing it in a controlled experiment. This approach therefore emerges as a promising tool to study systems where analytical and numerical techniques are not applicable. One of the most promising experimental setups for the purpose of quantum simulation are *cold atoms*, which will be introduced in the next section.

## 1.3 Cold Atoms

*This section offers a quick overview of some of the techniques used to implement lattice models of strongly correlated particles in cold atom experiments. I also introduce Rydberg and Rydberg-dressed atoms as a tool to engineer Hamiltonians with extended-range interactions. The results for bosonic systems discussed in this thesis are of interest for this kind of experiments.*

In the most basic cold atom experiment (for reviews see, e.g., [26, 27]) an ensemble of atoms (or molecules) confined in a trapping potential (usually of optical or magnetic nature) is cooled to very low temperatures, of the order of $10^{-6} \div 10^{-9}$ K. In these conditions, the quantum-mechanical properties of the atoms become important, allowing to directly observe macroscopic quantum effects such as Bose-Einstein condensation (BEC) ([28, 29, 30]) or superfluidity ([4, 31]).

In recent years, a great degree of controllability and tunability has been achieved in cold atom experiments. This kind of experimental setup has therefore become a great candidate for quantum simulation, with some realizations of the latter already achieved (including, e.g., the observation of the Superfluid-Mott Insulator transition in the Bose-Hubbard model [32]).

In particular, an important step made towards the experimental engineering of lattice Hamiltonians like the Hubbard or $t - J$ is the possibility to create *optical lattices*. The latter are periodic, lattice-like potentials for the atoms, constructed via the use of counter-propagating laser beams creating a standing wave. The light-matter interaction between the atoms and the interference pattern of the lasers generates an effective potential with regularly spaced regions of minimum potential energy. The latter act as effective lattice sites for the atoms, which may ”hop” between them if the energy barrier between two minima is low enough.

The depth of the potential minima, and therefore the strength of the

effective hopping amplitude, can be easily modified by changing the intensity of the laser beams, while changing their relative angle modifies the geometry of the potential (allowing to construct essentially any lattice structure).

In addition to the possibility of engineering lattice structures in a clean and controllable way, cold atoms are regarded as good systems for quantum simulation also due to the degree of control achievable on the interparticle interaction.

At low enough temperature, short-range interactions between neutral atoms in the ground state can be effectively approximated as an effective contact interaction $V_c(r) \sim a\delta(r)$, where $a$ is the atomic scattering length and $r$ is the interatomic distance. In many experiments this interaction can be widely tuned by taking advantage of a physical phenomenon called *Feshbach Resonance* (see, e.g., [33]). In this scenario, the low-energy scattering channel for the two-atom collision process energetically approaches another channel, which leads to the formation of a two-atom bound state. In the case most commonly employed in the experiments, the two channels have different magnetic moments, and can be resonantly coupled by a magnetic field $B$. The effect of this coupling can be described by an effective value of the atomic scattering length $a_{\text{eff}}(B)$, which can be tuned to have different sign and magnitude with respect to the off-resonant value $a$.

The possibility of tuning the interaction value allows the direct realization of phenomena such as the *BCS-BEC crossover* (see, e.g., [34] for a review, [35] for an experimental observation). In this scenario, the interactions in a fermionic system are tuned to pass from a BCS superconducting state (in the weakly attractive regime) to a BEC of difermionic molecules (in the strongly attractive regime).

An interesting recent avenue of research is the study of atomic and molecular systems interacting via extended-range potentials, which may in principle lead to the observation of novel physical phenomena. Available experimental platforms to this end include dipolar atoms [36], cold

molecules [37] and *Rydberg atoms*, on which the rest of this section will focus.

Rydberg atoms (see, e.g., [38, 39, 40]) i.e. atoms in states of high principal quantum number $n$, display several outstanding properties: for instance, a large atomic size (of the order of $10^{-6}$ m for $n \sim 100$), a long lifetime, scaling as $n^{-3}$, and a large dipole moment $\mu \sim n^2$.

Rydberg states of alkali metal atoms possess a rich fine and hyperfine structure, which make them highly tunable and addressable using external fields. This addressability can be used to engineer the interaction potentials between atoms. For example, the presence of an external electric field can induce permament electric dipole moments in the excited states, and the resulting Rydberg-Rydberg interaction scales as $r^{-3}$. In the absence of external fields, the dominant contribution is given by Van-der-Waals forces, scaling as $V(r) \sim C_6/r^6$ with $C_6 \sim n^{11}$. The resulting interactions are orders of magnitude larger than those in the between atoms in the ground state. Experimentally, the sign of these potentials can be changed utilizing different Rydberg states: in the following, repulsive Van-der-Waals interactions will be assumed. A further assumption which will be made in this section is the the description of Rydberg atoms as two-level systems with ground state $\mid g \rangle$ and excited state $\mid e \rangle$, driven by a laser of Rabi frequency $\Omega$ and detuning $\Delta$. In this section, and in the rest of the thesis, $\hbar = 1$ will be set.

Rydberg atoms allow to observe characteristic phenomena such as the *Rydberg Blockade*, i.e. the suppression of the simultaneous excitation of two atoms to the Rydberg state within a certain distance of each other. In a schematic picture, this is due to the fact that the energy level of the state of the system with two excited atoms is shifted of an amount given by the Rydberg-Rydberg interaction $V(r)$. In the case of red detuning (i.e. $\Delta < 0$) and for large enough shifting (i.e. for small enough $r$) the aforementioned level becomes off-resonance with respect to the laser used to drive the excitation. One can then define a *blockade radius* $r_b$ below which simultaneous excitations are forbidden. The energy level scheme of the blockade phenomenon is depicted in **Figure 1.1**.

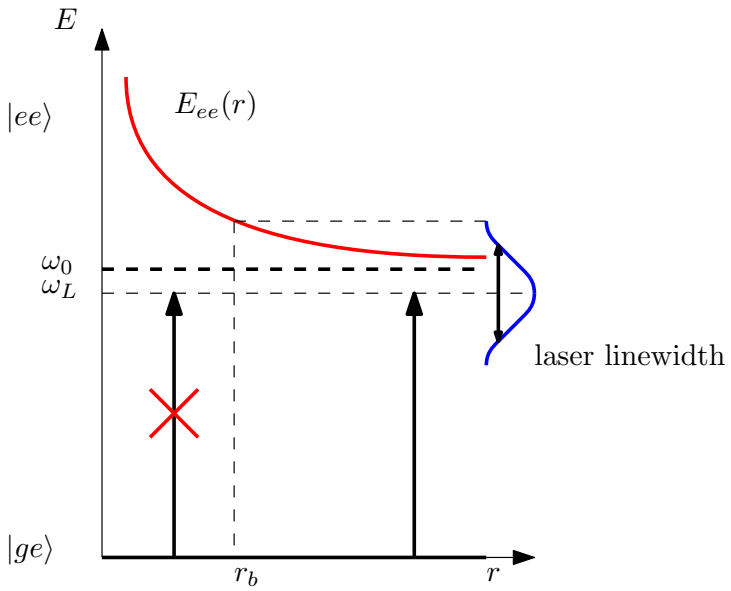


**Figure 1.1:** Energy level scheme for the Rydberg blockade phenomenon. The relevant states of the system are $\mid ge \rangle$ and $\mid ee \rangle$, with one and two excited atoms, respectively. Setting as zero the energy of the former, the energy of the latter becomes $E_{ee}(r) = \omega_0 + V(r)$ (red curve), where $V(r)$ is the Rydberg-Rydberg potential defined in the text and $\omega_0$ is the frequency of the Rydberg transition. The laser frequency is $\omega_L < \omega_0$ (i.e. red detuning).$r_b$ is the blockade radius. The transition from $\mid ge \rangle$ to $\mid ee \rangle$, mediated by a photon of frequency $\omega_L$ (black arrows) is allowed (suppressed) for $r > r_b$ ($r < r_b$) because the corresponding energy level $E_{ee}(r)$ lies inside (outside) of the laser linewidth (blue curve).

The Rydberg blockade phenomenon plays a crucial role in *Rydberg-dressed states* [41, 42, 43, 44, 45, 46, 47, 48, 49, 50]. The latter are superpositions of the ground state $\mid g \rangle$ and the excited (Rydberg) state $\mid e \rangle$ of the atom, which can be experimentally engineered via the use of laser beams. In the *far-off-resonant* regime ($\Omega \ll \Delta$), the ground-state of the atom-light Hamiltonian is a dressed state in the form

$$\mid d \rangle = \mid g \rangle + \alpha \mid e \rangle \qquad \alpha = \left(\frac{\Omega}{2\Delta}\right) \tag{1.1}$$

This kind of states has notable properties, such as a lifetime $\alpha^{-2}$ times longer than the bare excited Rydberg states. The interaction between Rydberg-dressed atoms in the far-off-resonant regime and for red

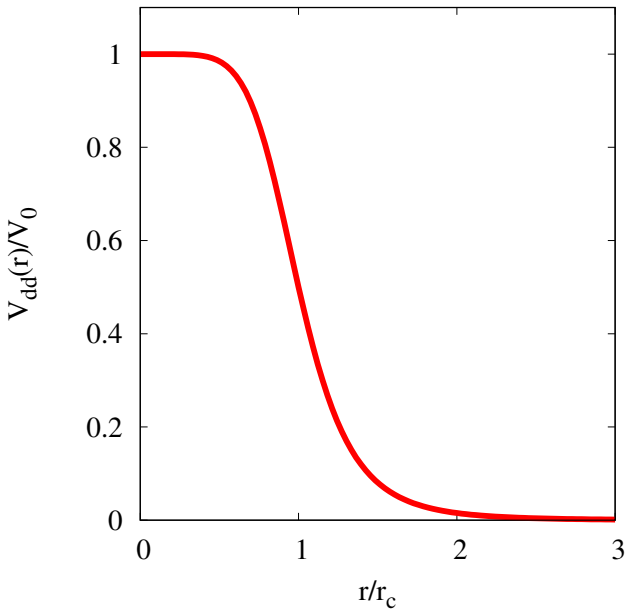


**Figure 1.2:** Two-body interaction (1.2) between Rydberg-dressed atoms as a function of the interatomic distance $r$.

detuning can be obtained via a perturbative expansion in $(\Omega/\Delta)$: the result up to sixth order [41, 51, 44] is the two-body potential

$$V_{dd}(r) = \frac{\left(\frac{\Omega}{2\Delta}\right)^4 C_6}{\left(\frac{C_6}{2|\Delta|}\right) + r^6} = \frac{V_0}{1 + \left(\frac{r}{r_c}\right)^6}, \tag{1.2}$$

with $V_0 = \Omega^4/8\Delta^3$ and $r_c = \sqrt[6]{C_6/2|\Delta|}$, represented in **Figure 1.2**, where $r$ is the interatomic distance. The experimental realization of this interaction between atomic spins has been reported [48, 49].

For large $r$, the interatomic potential (1.2) reduces to the Van-der-Waals interaction between excited Rydberg atoms, weighted by the probability $\alpha^4$ of exciting both atoms at the same time. For small $r$, instead, a blockade-like phenomenon strongly inhibits the probability of simultaneous excitation: the competition between this effect and the increase in $V(r)$ makes the interaction $V_{dd}(r)$ approach a constant value for $r \to 0$.

Due to the possibility of fine-tuning the details of the potential (1.2)

(by changing the laser parameters $\Omega$ and $\Delta$) as well as the aforementioned experimental realizability of Rydberg-dressed states, the latter are a promising tool for quantum simulation of systems with extended-range interactions.

The experimental realizability of Rydberg-dressed states has motivated the numerical study of systems interacting via the potential (1.2), demonstrating the appearance of physical phenomena of considerable interest, such as free-space supersolid phases described by the Andreev-Lifshitz-Chester mechanism [13]. One of the goals of this thesis is to proceed in this direction, investigating (via state-of-the-art numerical techniques) the existence of exotic many-body phenomena in systems of interest for experimental realizations with Rydberg-dressed atoms [14].

## 1.4 Outline of the Results

*This section contains a brief outline of the results exposed in the thesis. Subsection 1.4.1 focuses on the study, via PIMC simulations, of lattice systems of hardcore bosons of interest for Rydberg-dressed experimental setups. Subsection 1.4.2 outlines the results obtained, via VMC simulations, for the fermionic $t-J$ model in the presence of two holes. Subsection 1.4.3 outlines my work on Diagrammatic Monte Carlo.*

### 1.4.1 Equilibrium and Out-of-Equilibrium phases of Interaction-Blockade Gases on a lattice

In section 3.1 I present my results [14] for a model of strongly correlated hardcore bosons on a triangular lattice. The system is described by the Hamiltonian

$$\widehat{H} = -t \sum_{\{i,j\}} \left( \widehat{b}_i^\dagger \widehat{b}_j + \text{h.c.} \right) + \sum_{i<j; r_{ij} \leq r_c} V n_i n_j \tag{1.3}$$

where $\widehat{b}_i$ is the annihilation operator for a hardcore boson on the site $i$, $\widehat{n}_i = \widehat{b}_i^\dagger \widehat{b}_i$ is the occupation of the site $i$, $\{i,j\}$ denotes nearest-neighbor pairs, and $r_{ij}$ is the distance between sites $i$ and $j$. The density-density interaction in (1.3) yields a contribution $V > 0$ if two occupied sites lie within a distance $r_c$ of each other, and zero otherwise. This interaction reproduces the main features of the potential between Rydberg-dressed atoms (1.2).

My primary goal is to investigate the interplay of different order parameters, associated to various physical behaviors. In particular, I focus on superfluid, crystalline and glassy properties. Due to the lack of reliable analytical treatment for the model of my interest, I employ numerical methods to investigate the behavior of the system. In particular, I perform numerically exact PIMC simulations using Worm Updates [52], a state-of-the-art method for systems of unfrustrated bosons, which I introduce in section 2.2. I personally wrote the implementation

of the algorithm used in my work.

My simulations demonstrate the existence, for intermediate values of the interaction strength $V$, of an equilibrium supersolid phase, showing simultaneously structural order and superfluidity. The former vanishes for small $V$, leading to a homogeneous superfluid phase, while the latter disappears in the opposite limit, leading to a crystalline phase.

In order to investigate the out-of-equilibrium scenario, I perform simulated temperature quenches. The latter lead, in the large-$V$ regime, to the appearance of a disordered, inhomogeneous phase, i.e. a glass. For intermediate $V$, glassy physics coexists with a sizeable superfluid fraction: such a state is known as a *superglass* (the disordered equivalent of a supersolid).

As opposed to many studies demonstrating (super)glassy physics, in which this kind of phenomenon is generated via artificially-induced frustration (e.g. [53]), the Hamiltonian used in my work is translationally invariant and frustration-free. Here, glassy physics arises from the formation of self-assembled particle clusters, which induce an effective polidispersity in the system. Given the simplicity and generality of the model (1.3), the phases demonstrated in my study should be of direct experimental relevance for state-of-the-art experiments with Rydberg-dressed atoms in optical lattices.

I also study the model (1.3) with $r_c = 2\sqrt{2}$ on a square lattice, up to system sizes of $N = 48 \times 48$ and temperatures $T/t = 1/20$. Preliminary results [54] show for these parameters a phase transition between a SS and a disordered, non-superfluid phase where the density matrix shows a power-law decay for long distances. Large-scale and low-temperature simulations are currently running to understand if, e.g., structural order and superfluidity disappear at the same time or if an intermediate phase is present, and to investigate possible temperature and size dependences of the aforementioned physical picture.

### 1.4.2 Variational Studies of the $t-J$ model with two holes

In section 3.2 I present my results [21] on the study of the two-dimensional $t-J$ Hamiltonian,

$$\widehat{H} = -t \sum_{\{i,j\},\sigma} \left( \widehat{C}^{\dagger}_{i\sigma} \widehat{C}_{j\sigma} + \text{h.c.} \right) + J \sum_{\{i,j\}} \left( \widehat{\boldsymbol{S}}_i \cdot \widehat{\boldsymbol{S}}_j - \frac{\widehat{n}_i \widehat{n}_j}{4} \right) \qquad (1.4)$$

in the presence of two mobile holes. In (1.4), $\widehat{C}_{i\sigma}$ is the annihilation operator for a spin-$1/2$ fermion with spin component $\sigma$ on the site $i$, $\widehat{\boldsymbol{S}}_i$ is a shorthand notation for the spin projection operators on site $i$, i.e. $\widehat{\boldsymbol{S}}_i = \left( \widehat{\boldsymbol{S}}^x_i, \widehat{\boldsymbol{S}}^y_i, \widehat{\boldsymbol{S}}^z_i \right)$, $\widehat{n}_i = \sum_\sigma \widehat{C}^{\dagger}_{\sigma i} \widehat{C}_{\sigma i}$, $\{i,j\}$ denotes sum over nearest-neighbor sites, and double occupancy of lattice sites is forbidden.

I focus on a square lattice comprising up to $N = 256$ sites in the parameter range $0.4 \leq J/t \leq 2.0$. I perform my study using the Variational Monte Carlo (VMC) method with the EPS ansatz, both introduced in section 2.3.

Ground state energies are obtained via the optimization of a wave function in which the weight of a given configuration is expressed in terms of variational coefficients associated with square and linear entangled plaquettes. My estimates are in excellent agreement with exact results available for the $N = 16$ lattice.

By extending my study to considerably larger systems I find, based on the analysis of the long distance tail of the probability of finding two holes at spatial separation $r$, and on my computed two-hole binding energies, the existence of a two-hole bound state for all the values of $J/t$ explored here. It is estimated that $d$-wave binding of the two holes does not occur for $J/t < J_c/t \simeq 0.19$.

These results agree with the general picture provided by previous studies [55, 56, 57]. The numerical method used in my work, however, allows to obtain higher accuracy results with respect to the other approaches employed in the literature.

Given the offered accuracy, as well as the flexibility of the VMC method in conjunction with the EPS ansatz, this study is foundational to the extension of this approach in order to study other fermionic prob-

lems of considerable interest, such as the $t - J$ model (1.4) in the case of finite hole concentration, in which the physical picture is still unclear [58, 59, 60].

### 1.4.3 Diagrammatic Monte Carlo

In chapter 4 I expose my work on DMC (for an introduction on the method see, e.g., [22]). This numerical technique has been recently the subject of intense theoretical work (see, e.g., [61, 62] and references therein) and has seen applications to challenging problems such as, e.g., the determination of the phase diagram of the 2D Hubbard Model [63].

After introducing the general concepts behind the method, I offer details about my implementation of this algorithm, discussing the chosen approaches and outlining possible future developments.

# Chapter 2

# Numerical Methods

*This chapter contains a quick overview of the numerical methods used to obtain the results shown in chapter 3. Section 2.1 discusses the basic ideas underlying underlying Monte Carlo sampling, which are later used in sections 2.2 and 2.3 and chapter 4 to introduce the Path Integral, Variational and Diagrammatic Monte Carlo approaches, respectively.*

## 2.1 Monte Carlo Algorithms

In statistical physics, the thermodynamical mean value of an observable $O$ for a classical system is computed as

$$\langle O \rangle = \frac{\sum_C O(C) \exp\left(-\beta E(C)\right)}{\sum_{C'} \exp\left(-\beta E(C')\right)} = \sum_C O(C) \left( \frac{e^{-\beta E(C)}}{Z} \right) = \sum_C O(C) W(C) \tag{2.1}$$

where $C$ and $C'$ run over all the possible configurations of the system, $O(C), E(C)$ are the values of the observable and of the energy for the configuration $C$, respectively, $\beta = 1/T$ is the inverse temperature (here and in the rest of the thesis the Boltzmann constant will be set to 1), $Z$ is the partition function, and $W(C) = \exp(-\beta E(C))/Z$ will be referred to as *configuration weight*.

To reliably approximate the thermodynamic limit, mean values like (2.1) usually need to be computed at large enough system sizes. However, the dependence on the latter of the number of configurations is usually exponential (e.g., $2^N$ configurations for a system of $N$ spin-$1/2$). This in general dooms any attempt to compute sums like those in (2.1) exactly for sizes of interest.

*Monte Carlo methods* (for a general introduction see, for instance, [64]) compute (2.1) via *stochastic sampling*, estimating $\langle O \rangle$ as the average of the contributions given by a large enough set of randomly selected configurations. The contribution $O(C)$ of each configuration $C$ is weighted in the average with the configuration weight $W(C)$.

The advantage in using stochastic sampling is that the estimate will asymptotically converge to the exact result, with a statistical uncertainty which scales asymptotically with the number of sampled configurations $M$ as $M^{-1/2}$. The uncertainty is therefore independent on the system size (which may however influence the time required to reach the asymptotic regime). This usually allows to analyze systems large enough to obtain a reliable approximation of the thermodynamic limit.

Sampling uniformly-distributed configurations may result in slow convergence to the exact result if the weight function $W(C)$ is sharply peaked (as in the case of (2.1)), because most sampled configurations will have small weight. A more efficient approach is to sample configurtions distributed according to the weight function $W(C)$, interpreted as a distribution. This naturally yields more often configurations with larger weight.

In the most commonly used family of Monte Carlo methods, known as *Markov chain Monte Carlo* approaches, this task is performed by creating a Markov chain of configurations sampled according to the weight function. Each element of the chain is generated from the previous one via application of modifications called *updates*: the transition from a configuration $C_1$ to any configuration $C_2$ has a probability $P(C_1 \to C_2)$ to happen. Two conditions are usually imposed in this process:

- The *detailed balance* condition is a relation involving the transi-

tion probability, which ensures the configurations will be sampled according to the weight function $W(C)$. It is a sufficient condition (less stringent ones can in principle be found) which reads

$$\frac{P(C_1 \to C_2)}{P(C_2 \to C_1)} = \frac{W(C_2)}{W(C_1)} \tag{2.2}$$

Usually the transition probability $P(C_1 \to C_2) \equiv P_{12}$ is decomposed as the product of a *proposition* probability $A_{12}$ (selecting the particular update that will lead from $C_1$ to $C_2$) and an *acceptance* probability $Q_{12}$ (the probability of actually performing the change). A possible choice of $Q_{12}$ respecting the condition (2.2) is the one employed in the *Metropolis-Hastings (MH) sampling* [65],

$$Q_{12} = \min\left(1, \frac{A_{21}W(C_2)}{A_{12}W(C_1)}\right) \tag{2.3}$$

Accepting or rejecting the update with probability (2.3) ensures the configurations in the Markov chain are asymptotically distributed according to $W(C)$. Since this expression only contains ratios of configuration weights, it is not required to compute the partition function present in the definition of the weight function (2.1), simplifying the sampling considerably.

- In order to sample the configuration space properly, the selected set of updates must be *ergodic*: any configuration must be reachable from any other through a finite number of updates. If an update scheme is not ergodic, sectors of the configuration space may not be sampled, yielding incorrect results.

Since the configuration weight is already kept into account in the choice of the configurations, (2.1) is simply approximated as

$$\langle O \rangle \cong \frac{\sum_{C \in \{C_1,\ldots,C_M\}} O(C)}{M} \tag{2.4}$$

where the sum is performed over configurations chosen via a MH process according to the distribution $W(C)$.

*Quantum Monte Carlo* approaches are techniques which study the behavior of quantum systems via stochastic sampling of quantities of interest. Some of the latter work at finite temperature, like Path Integral Monte Carlo (PIMC), which will be discussed in section 2.2, while others work in the ground state, such as Variational Monte Carlo (VMC), introduced in section 2.3.

## 2.2 Path Integral Monte Carlo

In order to introduce the PIMC method, it will be supposed, without loss of generality, that the system of interest is bosonic, and described by a lattice Hamiltonian

$$\widehat{H} = \underbrace{\sum_{i,j=1}^{N} U_{ij}\widehat{n}_i\widehat{n}_j}_{\widehat{H}_0} + \underbrace{\sum_{i,j=1}^{N} V_{ij}\widehat{b}_i^\dagger\widehat{b}_j}_{\widehat{V}} = \widehat{H}_0 + \widehat{V} \tag{2.5}$$

where $N$ is the number of sites, $\widehat{b}_i$ is the bosonic annihilation operator on site $i$ and $\widehat{n}_i = \widehat{b}_i^\dagger\widehat{b}_i$. It will also be assumed that $V_{ij} \leq 0$ for all $i, j$, as well as periodic boundary conditions in space.

The starting point of PIMC algorithms (see for instance [52, 66]) is the expansion of the partition function $Z$ for the quantum system as

$$Z = \sum_{n=0}^{\infty}\int_0^\beta d\tau_n \int_0^{\tau_n} d\tau_{n-1}\ldots\int_0^{\tau_2} d\tau_1 \ \mathrm{tr}\left[(-1)^n e^{-\beta\widehat{H}_0}\widehat{V}(\tau_n)\ldots\widehat{V}(\tau_1)\right] \tag{2.6}$$

Where $\tau \in [0, \beta]$, tr denotes the trace over the Hilbert space, and $\widehat{V}(\tau) = e^{\tau\widehat{H}_0}\widehat{V}e^{-\tau\widehat{H}_0}$. Inserting sums over the set of eigenvectors $\mathcal{S}$ of, e.g., the site occupation operators $\widehat{n}_i$ allows to rewrite the trace in (2.6) as

$$\sum_{|\,i_0\,\rangle,\ldots,|\,i_{n-1}\,\rangle\in\mathcal{S}} W\left(|\,i_0\,\rangle, \tau_1, |\,i_1\,\rangle, \tau_2, \ldots, |\,i_{n-1}\,\rangle, \tau_n\right) \tag{2.7}$$

where

$$\begin{aligned}
&W\left(|\,i_0\,\rangle, \tau_1, |\,i_1\,\rangle, \tau_2, \ldots, |\,i_{n-1}\,\rangle, \tau_n\right) = (-1)^n \left\langle i_0 \right| e^{-\beta\widehat{H}_0}e^{\tau_n\widehat{H}_0}\widehat{V}e^{-\tau_n\widehat{H}_0} \left| i_{n-1} \right\rangle \times \\
&\times \left\langle i_{n-1} \right| e^{\tau_{n-1}\widehat{H}}\widehat{V}e^{-\tau_{n-1}\widehat{H}_0} \left| i_{n-2} \right\rangle \times \ldots \times \left\langle i_1 \right| e^{\tau_1\widehat{H}_0}\widehat{V}e^{-\tau_1\widehat{H}_0} \left| i_0 \right\rangle \\
&= e^{-(\tau_1-\tau_n+\beta)E_0} \left\langle i_0 \right| \widehat{V} \left| i_{n-1} \right\rangle e^{-(\tau_n-\tau_{n-1})E_{n-1}} \left\langle i_{n-1} \right| \widehat{V} \left| i_{n-2} \right\rangle \times \\
&\times e^{-(\tau_{n-1}-\tau_{n-2})E_{n-2}} \left\langle i_{n-2} \right| \widehat{V} \left| i_{n-3} \right\rangle \ldots e^{-(\tau_2-\tau_1)E_1} \left\langle i_1 \right| \widehat{V} \left| i_0 \right\rangle
\end{aligned} \tag{2.8}$$

In (2.8), the exponential terms can be interpreted as Schrödinger time-evolution operators in the *imaginary time* $\tau = it$ between the states $|\, i \,\rangle$ at times $0 < \tau_1 < \ldots < \tau_n < \beta$; at these times, the hopping operators $\widehat{V}$ are applied, changing the site occupations and therefore the state. The evolution follows periodic boundary conditions in time (i.e., the states at $\tau = 0$ and $\tau = \beta$ must be identical). Due to the choice of $V_{ij} \leq 0$, (2.8) is always positive.

To simplify the notation, a *configuration* $C$ *of order* $n$ will be defined as the set of $n$ states $\{|\, i_0 \,\rangle, \ldots, |\, i_{n-1} \,\rangle\}$ and $n$ times of application of the nondiagonal operators $\{\tau_1, \ldots, \tau_n\}$ which define each term of the sum in (2.7). The function $W$ in (2.8) will be referred to as *configuration weight*. Combining (2.6), (2.7) and (2.8), the partition function then becomes

$$Z = \sum_{n=0}^{\infty} \sum_{C \in \mathcal{L}_n} W(C) \tag{2.9}$$

where $\mathcal{L}_n$ is the set of all configurations of order $n$.

A configuration can be graphically represented as in **Figure 2.1**. The red lines in the figure, marking the evolution in space and time of the particles, are known as *worldlines*. *Kinks* (points in which the system state changes, and worldlines move between sites) correspond to the application of an operator $\widehat{V}$.

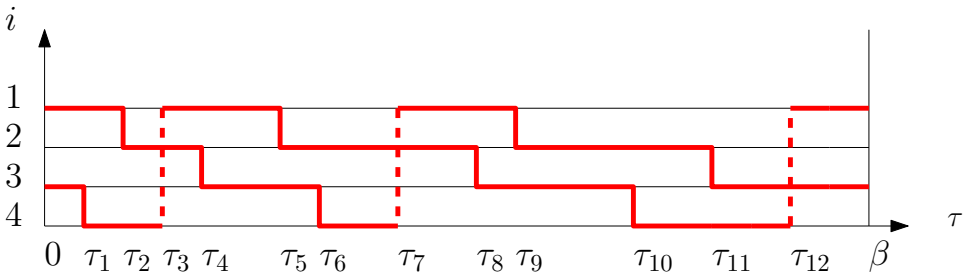


**Figure 2.1:** Graphical representation of a configuration on a 4-site chain for the Hamiltonian (2.5) with nearest-neighbor hopping. $i$ marks the site index. The worldlines (red lines) mark the occupied sites at each imaginary time. The times at which hopping operators are applied are marked. The dashed line marks a jump which wraps around the system.

In this representation, quantum effects become geometrical features of the configuration. For instance, particle exchanges are represented by worldline permutations between the states at $\tau = 0$ and $\tau = \beta$ (as in **Figure 2.1**). Due to the indistinguishability of the particles, these exchanges do not break the periodic boundary conditions in time, as long as the state does not change.

Through repeated particle exchanges, worldlines can wind around the periodic boundary conditions in space. The number of times worldlines wrap around the system is known as *winding number*, and is connected to the presence of superfluidity: for instance, the configuration shown in **Figure 2.1** has winding number $w = 3$.

In this formalism, in order to compute the thermodynamical mean value for an observable $\widehat{O}$, i.e.

$$\left\langle \widehat{O} \right\rangle = \frac{\mathrm{tr}\left(\widehat{O} e^{-\beta \widehat{H}}\right)}{Z} \tag{2.10}$$

one can expand (2.10) in the same way used for the partition function, obtaining expressions similar to (2.6) – (2.8) (the only difference is the presence of an additional $\widehat{O}$ in one of the matrix elements).

Assuming $\widehat{O}$ to be diagonal on the set $\mathcal{S}$, and performing the same steps used to obtain (2.9), the mean value of $\widehat{O}$ becomes

$$\left\langle \widehat{O} \right\rangle = \sum_{n=0}^{+\infty} \sum_{C \in \mathcal{L}_n} \widehat{O}_C P(C) \tag{2.11}$$

where $P(C) = W(C)/Z$ and $\widehat{O}_C = \left\langle i_k \,|\, \widehat{O} \,|\, i_k \right\rangle$ is the mean value of the operator on one of the states of the configuration (due to the cyclic property of the trace, all choices are equivalent).

The sum over the configurations in (2.11) is usually impossible to compute exactly for large enough system sizes to reliably approximate the thermodynamic limit. PIMC methods compute (2.11) via stochastic sampling: in particular, configurations are sampled via a MH process (see section 2.1) according to the function $P(C)$ in (2.11). The updates of the MH process change the position in time of the kinks, their number

and the sites they link. Usually, instead of computing the quantity $\widehat{O}_C$ in (2.11) on a single state of $C$, the average in $\tau$ of the mean values of $\widehat{O}$ computed on all states is used to improve the collected statistics.

The updates chosen for the MH process have to conserve periodic boundary conditions in $\tau$: with this restriction, the simplest possible moves are the insertion of pairs of kinks in which a particle jumps from a site to another and back, or the motion in time of a kink. However, this simple set of updates is not ergodic, since it cannot change the net winding number of the system. More sophisticated updates are therefore required to measure important quantities such as the superfluid density.

An example of ergodic update scheme are the *worm updates* [52]. The first update of the worm scheme creates an *open* worldline, by "deleting" a part of a worldline [as shown in panel (a) of **Figure 2.2**] or by inserting a new worldline with open ends. The discontinuities created in this fashion in the worldlines are named *worm heads*.

After the insertion, updates may move the worm heads in time [panel (b) of **Figure 2.2**] or in space: the latter movement may result in particle exchanges being performed [panel (d)] or not [panels (c) and (e)]. If the two worm heads are on the same site, and no kinks are between them, an update may be performed to "close" the worm [panel (f)].

Using worm updates, two configurations spaces are sampled simultaneously:

- The configurations where the worm is closed are weighted according to (2.8), and allow to measure observables like the site occupation $\widehat{n}_i$ and the density-density correlations $\widehat{n_i n_j}$. These in turn give access to quantities like the total density ($\rho = N^{-1} \sum_i \langle \widehat{n}_i \rangle$), the potential energy ($\langle U \rangle = \sum_{ij} U_{ij} \langle \widehat{n_i n_j} \rangle$) or the structure factor $S(\boldsymbol{k})$ (the Fourier transform of the density-density correlations). The latter is connected to the presence of structural order in the system.

  Some nondiagonal operators can also be computed via this expression, if they are connected to another diagonal operator or quantity

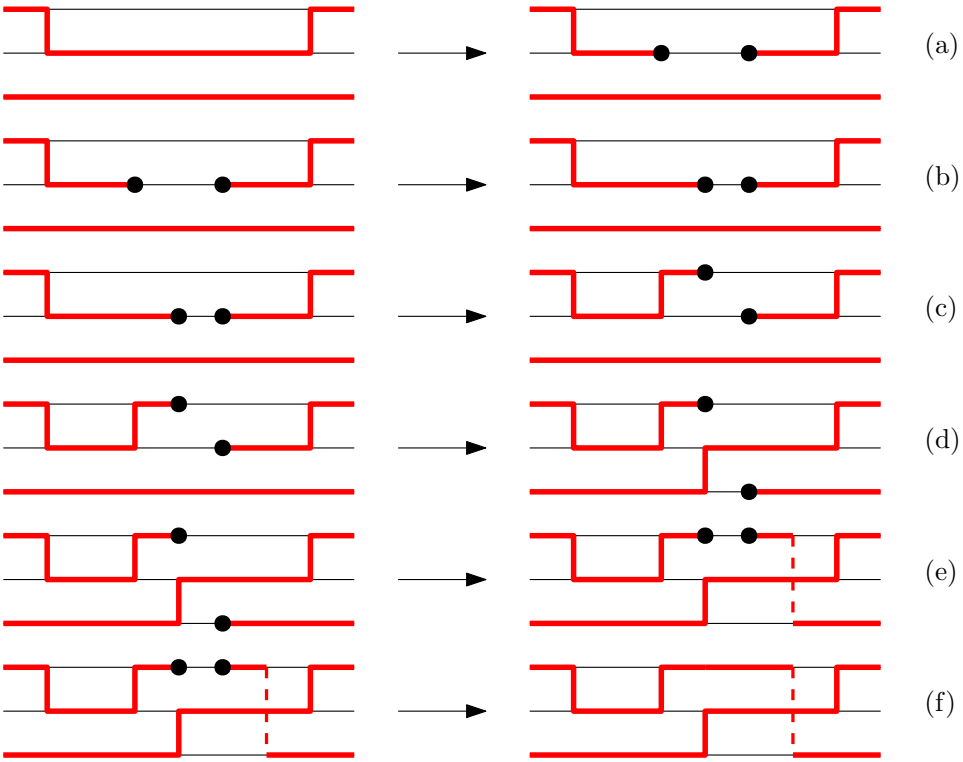


**Figure 2.2:** Example updates in the worm scheme. Jumps wrapping around the system are denoted by dashed lines. The black dots are the worm heads. The final configuration for each panel is the starting configuration for the following one.

which can be measured in their place. For instance, the kinetic energy $K$, the mean value of the operator $\widehat{V}$, can be easily computed since it is related to the average number of kinks $\langle N_k \rangle$ as $K = -\langle N_k \rangle / \beta$.

The superfluid fraction $\rho_s$, which indicates the percentage of particles involved in superfluid motion, can also be straightforwardly measured as a function of the squared winding number $w^2$ (usually averaged over the spatial directions). The proportionality constant depends on the dimensionality and on the lattice geometry: e.g., for a system described by the Hamiltonian (2.5) with hopping restricted to nearest-neighbor sites and uniform hopping coefficient $t$ on a hypercubic lattice in $d$ dimensions [67],

$$\rho_s = \frac{1}{\rho} \frac{\langle w^2 \rangle N^{\frac{2-d}{d}}}{2t\beta} \tag{2.12}$$

- When the worm is open, i.e. for discontinuous worldlines, the configuration contributes to the partition function of a different configuration space, given by

$$Z_G = \mathrm{tr}\left[T_\tau \left(\widehat{b}_i(\tau_1)\widehat{b}_j^\dagger(\tau_2)e^{-\beta\widehat{H}}\right)\right] \tag{2.13}$$

  $T_\tau$ denotes a time-ordered product in imaginary time (operators are ordered, via commutations, from left to right with decreasing $\tau$). The two Fock operators correspond to the two worm heads. The same expansion used for the partition function can be performed here, leading to a configuration weight with the same structure of (2.8) but two additional states at each order, generated by the application of the worm head operators, and the corresponding matrix elements. The MH process for the worm updates is performed using this extended configuration weight.

  Sampling of this extended configuration space allows to measure the *single particle imaginary time Green function*, defined as

$$G(i,j,\tau_1,\tau_2) = -\left\langle T_\tau \left(\widehat{b}_i(\tau_1)\widehat{b}_j^\dagger(\tau_2)\right)\right\rangle \tag{2.14}$$

  which is difficult to measure using other update schemes. Furthermore, relaxing the condition of having continuous worldlines allows to naturally create long particle-exchange cycles with nonzero winding number, as in **Figure 2.2**. These cycles will remain in the configuration when the worm is closed, ensuring an ergodic sampling of the configuration space.

  Worm updates also allow to naturally work in the grandcanonical ensemble, since the worm closure can happen at a different particle number than the worm creation (canonical results can be obtained by only measuring closed-line observables when the particle number has the desired value).

The PIMC method with worm updates is a state-of-the-art numerical technique which allows to reliably approximate the thermodynamical limit in a large number of systems, both for $T > 0$ and in the ground state (via extrapolation to $T = 0$). Furthermore, the results of this approach are *numerically exact*, i.e. they are free from systematic errors and biases, converge to the exact result in the limit of infinite simulation, and the uncertainty on the results can be reduced at will by simply increasing the number of sampled configurations (i.e., the simulation time).

For these reasons, PIMC with worm updates has been chosen as the method of investigation for my work on bosonic systems illustrated in section 3.1. The implementation of the algorithm used in this study has been written by myself.

PIMC, however, encounters severe difficulties when applied to systems of bosons or spins with positive hopping terms (usually referred to as *frustrated*) and fermions, due to the presence of positive matrix elements of the nondiagonal term $\widehat{V}$ in (2.8). These result in some configurations having negative weight: since the MH procedure uses the weight function as a part of the acceptance probabilities, stochastic sampling cannot be directly performed. This issue is referred to as *sign problem* (see, e.g., [20] for an introduction) and can in principle be treated using numerical workarounds: however, the latter cause heavy numerical instabilities, and ultimately fail to provide reliable results at large sizes and low temperatures.

Numerical techniques which do not suffer from the sign problem are therefore important tools to study systems of frustrated bosons and fermions. Two such approaches (namely, Variational Monte Carlo and Diagrammatic Monte Carlo) will be introduced in sections 2.3 and chapter 4, respectively.

## 2.3 Variational Monte Carlo

VMC (see, e.g., [68] for a review) is a numerical approach which allows to investigate the ground state (GS) properties of a given model Hamiltonian. Without loss of generality, I will consider a collection of $N$ spin-$1/2$ on an $N$-site lattice. Provided a trial state $\mid \psi \rangle$, expressed as a weighted superposition of all possible system configurations $\mid \boldsymbol{m} \rangle = \mid S_z^1, \ldots, S_z^N \rangle$ as

$$\mid \psi \rangle = \sum_{\boldsymbol{m}} W(\boldsymbol{m}) \mid \boldsymbol{m} \rangle \tag{2.15}$$

the expectation value of the Hamiltonian on $\mid \psi \rangle$ can be written as

$$E = \frac{\sum_{\boldsymbol{m}} W^2(\boldsymbol{m}) E_L(\boldsymbol{m})}{\sum_{\boldsymbol{m}'} W^2(\boldsymbol{m}')} = \sum_{\boldsymbol{m}} P(\boldsymbol{m}) E_L(\boldsymbol{m}) \tag{2.16}$$

where the *local energy* $E_L(\boldsymbol{m})$ is defined as

$$E_L(\boldsymbol{m}) = \sum_{\boldsymbol{m}''} \frac{W(\boldsymbol{m}'')}{W(\boldsymbol{m})} \left\langle \boldsymbol{m}'' \mid \widehat{H} \mid \boldsymbol{m} \right\rangle \tag{2.17}$$

and

$$P(\boldsymbol{m}) = \frac{W^2(\boldsymbol{m})}{\sum_{\boldsymbol{m}'} W^2(\boldsymbol{m}')} \tag{2.18}$$

Here $W(\boldsymbol{m}) = W^*(\boldsymbol{m})$ is assumed for simplicity. According to the variational principle, for any choice of weights $E$ is an upper bound of the GS energy: the best possible approximation to the latter can be found by minimizing (2.16) with respect to the weights $W$.

Usually, due to the large number of system states $\mid \boldsymbol{m} \rangle$, the sum in (2.16) cannot be computed exactly. In VMC, the latter are estimated via stochastic sampling: in particular, a MH process (see section 2.1) is employed to sample the states $\mid \boldsymbol{m} \rangle$ with respect to the function $P(\boldsymbol{m})$ in (2.18). Since the latter is always positive, VMC methods do not suffer from the sign problem.

Once the optimization process for the weights is terminated, observables can be computed by decomposing their mean value in a similar

fashion to (2.16).

In this method, the choice of ansatz is crucial to obtain accurate results. A good trial WF should be systematically improvable and easy to program. The one used in this thesis is the *Entangled Plaquette States* (EPS), introduced in [69].

The general idea of the EPS ansatz is to express the weight $W(\boldsymbol{m})$ of a generic global configuration $\mid \boldsymbol{m} \rangle$ in terms of variational coefficients in biunivocal correspondence with the configuration of different groups of sites i.e., plaquettes.

The simplest (non entangled) plaquette ansatz consists in choosing

$$W(\boldsymbol{m}) = \prod_{P=1}^{N} C_P^{m_{i_{1,P}}} \tag{2.19}$$

where the $C_P^{m_{i_{1,P}}}$ are variational coefficients associated with the configuration of the single site, labeled by $m_{i_{1,P}}$, of the $P_{th}$ plaquette. This choice results in a mean-field-like WF where correlations are neglected. However, they can be promptly incorporated in the ansatz by increasing the plaquette size. While in the case of non overlapping plaquettes correlations are well described for distances of the order of the plaquette size, a reliable description of long range correlations is obtainable, even with relatively small plaquettes, when the latter overlap (i.e., are entangled). Clearly, any EPS ansatz is a legitimate variational choice regardless of the size of the plaquette used.

In other words, one can adopt a given plaquette size and provide variational estimates with an accuracy related to the given dimension of the plaquettes. The EPS WF is systematically improvable by enlarging the size of the plaquettes and/or by including plaquettes of various shapes correlating specific groups of sites, being exact in the limit of a single plaquette as large as the system.

This trial wavefunction has been used to study quantum antiferromagnets [70, 71] and fermionic Hamiltonians such as the $t-J$ model in the presence of one mobile hole [72]. VMC with the EPS ansatz allowed to obtain results of comparable or better accuracy than those obtainable

with other wavefunctions or variational techniques for these problems.

My work on fermionic systems [21] illustrated in section 3.2 aims to apply this ansatz to the $t - J$ model in the presence of two holes, where most other techniques suffer from different limitations or require approximations. Also in this case, the results I obtain are of accuracy comparable or better than those in the literature. This confirms the validity of the EPS ansatz which, due to its flexibility, can be adapted to study some of the most interesting and challenging lattice models, such as, e.g., the $t - J$ model at finite hole concentration.

# Chapter 3

# Results

*This chapter contains an in-depth discussion of the results of my studies. In particular, section 3.1 is devoted to my investigation of lattice systems of hardcore bosons [14, 54] while section 3.2 discusses my work on the fermionic $t-J$ model in the presence of two holes via VMC simulations with the EPS ansatz [21].*

## 3.1 Equilibrium and Out-of-Equilibrium phases of Interaction-Blockade Gases on a lattice

It is well established that bosonic and fermionic systems subjected to a disordered external potential feature localization phenomena [73, 74]. The interplay between disorder, interactions and many-body quantum effects such as superfluidity is now a subject of intense research [75, 76, 77], as, e.g., bosons in random environments occur in a variety of experimentally relevant systems ranging from cold atoms [78, 79, 80, 81, 82], to superconductors [83] and quantum liquids [84]. Usually, the combination of disorder and repulsive interactions inhibits the emergence of superfluidity and Bose-Einstein condensation (BEC) and leads to an insulating gapless phase, known as Bose glass [85, 86, 87].

Remarkably, results of quenched Monte Carlo simulations in the

context of $^4$He have shown that superfluidity and BEC may coexist with structural disorder and inhomogeneity (i.e., glassy physics) in the absence of any random external potentials [88]. The resulting out-of-equilibrium state was termed *superglass* (SG), as a disordered analog of the supersolid (SS) phase [3]. While experiments have so far remained inconclusive [89, 90], this proposal has spurred considerable theoretical activity to derive possible microscopic models of a SG [91, 53, 92, 93]. Exact numerical results for bosons on lattices have shown that a thermodynamic SG phase can indeed emerge as a result of a competition of quantum fluctuations and externally induced frustration. For attractive interactions the latter can be induced via a random chemical potential [92], while for repulsive ones a SG can occur in theoretical models where either a self-disordered environment is induced by geometrical frustration (e.g., on random graphs) [53] or where disorder is a consequence of properly chosen random inter-particle interactions [93]. In this context, main open questions are whether it is possible to obtain a SG in any theoretical models where frustration is not artificially built in the Hamiltonian, and if this new phase of matter may be experimentally observable in any physical system.

In my work [14] I show that the SG phase can exist for a large class of bosonic lattice Hamiltonians. The latter are of the extended Bose-Hubbard type, featuring a soft-shoulder interaction potential. Surprisingly, glassy behavior is obtained in the absence of any externally imposed frustration e.g., in the lattice geometry, or in the interactions. Rather, frustration is here induced by cluster formation for large particle density, similar to the conditions of SS formation in soft-core models [41, 42]. As an example, I consider a simple triangular lattice with isotropic two-body interactions. I analyze the phases and, following a quench in the temperature $T$ or in the interaction strength, demonstrate the existence of both a glass (G) and a SG at low enough $T$. The latter are the out-of-equilibrium counterparts of a floating stripe solid (S) and a SS, respectively. These glass and superglass phases should be observable in experiments with Rydberg-dressed alkali atoms loaded into optical lattices.

The relevant Hamiltonian for hard-core bosons on a triangular lattice reads

$$\widehat{H} = -t \sum_{\{i,j\}} \left( \widehat{b}_i^\dagger \widehat{b}_j + \text{h.c.} \right) + \sum_{i<j; r_{ij} \leq r_c} V n_i n_j \tag{3.1}$$

Here the $\widehat{b}$ are the annihilation operators for hardcore bosons, $\widehat{n}_i = \widehat{b}_i^\dagger \widehat{b}_i$ is the occupation of the site $i$, $\{i,j\}$ denotes nearest-neighbor pairs, and $r_{ij}$ is the distance between sites $i$ and $j$. The lattice spacing $a$ and the tunneling rate $t$ are used as units of energy and length, respectively. The step-wise interaction in (3.1) (which yields a contribution $V > 0$ if two occupied sites lie within a distance $r_c$ of each other, and zero otherwise) aims to reproduce the main features of the interaction (1.2) between two Rydberg-dressed atoms discussed in section 1.3. It will be later shown that using the full potential (1.2) does not change the physical picture. The additional onsite hard-core constraint can be enforced using, e.g., Feshbach resonances.

The quantum phases of (3.1) with $r_c = 1$ (i.e., nearest-neighbor interactions) are well known [94, 95, 96, 97, 12]: for densities $\rho < 1/3$ ($\rho > 2/3$), $\rho = 1/3$ ($\rho = 2/3$) and $\rho > 1/3$ ($\rho < 2/3$) the low-energy phase is a superfluid (SF), a gapped lattice S, or a gapless SS, respectively. The latter is an exotic state of matter where density correlations (here with $\sqrt{3} \times \sqrt{3}$ ordering) coexist with a finite superfluid fraction $\rho_s$, which is a result of doping the solid with interstitials (vacancies). The SS phase is generally robust against perturbations to the Hamiltonian (3.1), and may be observed experimentally, e.g., with cold quantum gases trapped in optical lattices and interacting via dipolar interactions [98, 99, 100].

I study the Hamiltonian (3.1) for $r_c > 1$. In this parameter range, the interaction in (3.1) belongs to a large class of potentials that support the formation of *clusters* of particles for density $\rho$ such that $r_c\sqrt{\rho} > 1$ [101, 102]. Such a phenomenon is essentially independent of the details of the interactions, as long as the latter display a negative Fourier component [103]. In the classical regime (i.e., $t = 0$) cluster formation has been shown to lead to frustration, which is manifested in an exponen-

tial growth of the ground state degeneracy as a function of the system size [104]. In the quantum regime (i.e., $t > 0$) this leads to several novel exotic phenomena at equilibrium: anomalous Luttinger-Liquid behavior [104] and emergent supersymmetry in 1D lattice geometry [105] as well as free-space supersolidity in 2D [13, 41, 42]. The latter occurs, for appropriate values of interaction strength, at any density fulfilling the clusterization condition $r_c\sqrt{\rho} > 1$ [13]. In the following I consider, as a way of example, the simplest cluster forming potential with $r_c = 2$ and incommensurate particle densities consistent with such a condition. My main focus is the demonstration of a G and SG emerging when a crystal and a SS are driven out of equilibrium via a temperature quench, respectively. Glassy phases for different $\rho$, $r_c$ and quench protocols are also discussed.

I study the Hamiltonian in (3.1) by means of PIMC simulations based on the worm algorithm: this method has been described in section 2.2. The implementation of the algorithm used in the calculations has been written by myself. This technique is numerically exact for bosonic systems and allows for accurate estimates of the superfluid fraction on the triangular lattice

$$\rho_s = \frac{\left\langle w_x^2 + w_y^2 \right\rangle}{6\beta\rho} \tag{3.2}$$

and the static structure factor

$$\frac{S(\boldsymbol{k})}{N} = \frac{1}{N^2}\sum_{i,j} e^{-i\boldsymbol{k}\cdot(\boldsymbol{r}_i - \boldsymbol{r}_j)} \left\langle \widehat{n_i n_j} \right\rangle \tag{3.3}$$

The latter measure superfluidity and diagonal crystalline order, respectively. Here, $N$ is the number of sites, $\beta = 1/T$ is the inverse temperature, $w_i$ is the winding number in the $i$-th direction, $\boldsymbol{k}$ is a lattice wavevector, and $\langle \ldots \rangle$ stands for statistical average. In addition, I compute the renormalized Edwards-Anderson order parameter $\widetilde{q}_{EA} = q_{EA}/q_{EA}^{\max}$, which, in the absence of crystalline order, is the well-accepted observable to identify glassy behavior on a lattice [53, 106]. Here,

$$q_{EA} = \sum_{i=1}^{N} \langle \widehat{n}_i - \rho \rangle^2 \tag{3.4}$$

and $q_{EA}^{\max} = N\rho(1-\rho)$ is its maximum value, obtained for a perfectly localized system. I perform large-scale simulations with up to $N = 2304$ lattice sites and temperatures as low as $T/t = 1/12$. For each $N$ and $T$, numerical values for the observables above are obtained by averaging over a minimum of 32 and a maximum of 100 different realizations of the quench.

Panel (a) of **Figure 3.1** shows example results for the superfluid fraction $\rho_s$ and the renormalized Edwards-Anderson parameter $\widetilde{q}_{EA}$ as a function of the interaction strength $V/t$ for $N = 900$ and $T/t = 1/12$. Within the interesting range of interaction ($5.0 \lesssim V/t \lesssim 6.0$), $\rho_s$ is found to decrease monotonically with increasing $V/t$ from approximately $0.25$ to about $0.05$. In the same parameter range, $\widetilde{q}_{EA}$ increases up to values of the order of $\sim 0.2$. I remark that in this regime the system does not feature crystalline order, i.e., the computed structure factor $S(\boldsymbol{k})/N$ vanishes for any non trivial wave vector $\boldsymbol{k} \neq 0$ in the thermodynamic limit, as proven in the inset of **Figure 3.1**, where I show the scaling with $N^{-1/2}$ of $S_{\max}/N$, the average of the largest peaks of the structure factor over several quench realizations. In the same limit the superfluid fraction and the Edwards-Anderson parameter remain finite and show a finite coexistence region.

These data demonstrate one of the main results of my study, namely the existence, in an extended region of parameters, of a SG, corresponding to an *inhomogeneous non-crystalline superfluid*. The dependence on $T/t$ of both $\widetilde{q}_{EA}$ and $\rho_s$ is shown in panel (b) of **Figure 3.1**. For the specific value of the interaction strength in the panel superglassiness is realised below $T/t \simeq 0.2$.

For weak interactions, the SG phase *quantum melts* into a regular homogeneous superfluid (SF) with $\rho_s > 0$ and $\widetilde{q}_{EA} \simeq S(\boldsymbol{k}) = 0$. For the parameters of panel (a) of **Figure 3.1** this is obtained by decreasing the interaction strength below $V/t \simeq 4.8$. On the other hand, sufficiently large interaction strengths are found to inhibit superfluidity and turn

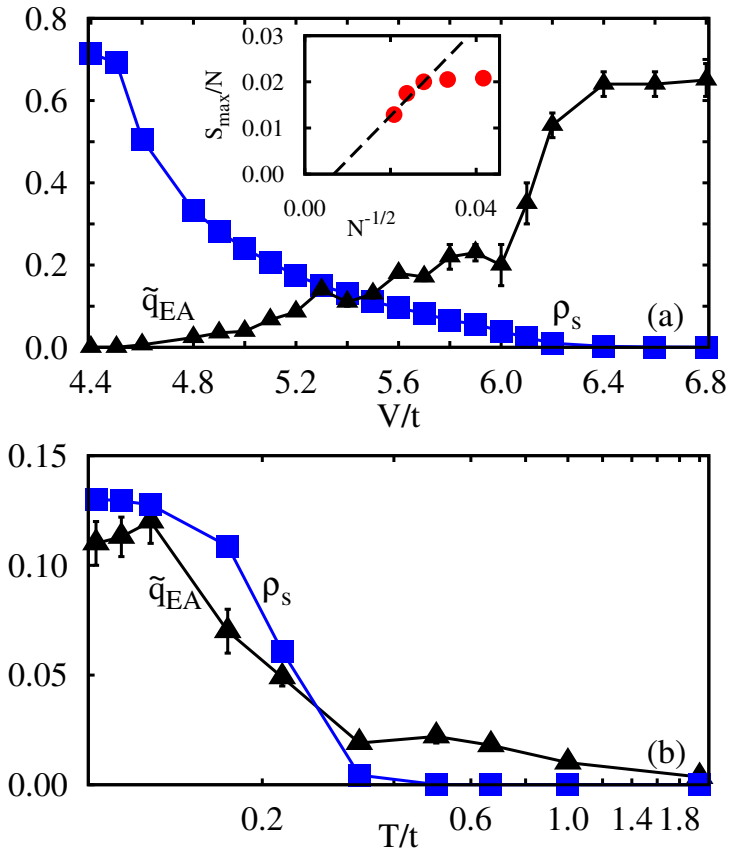


**Figure 3.1:** (a): Superfluid fraction $\rho_s$ and renormalized Edwards-Anderson parameter $\widetilde{q}_{EA}$ as a function of $V/t$, for $T/t = 1/12$. (b): $\rho_s$ and $\widetilde{q}_{EA}$ as a function of $T/t$, for $V/t = 5.4$. In both panels the density is $\rho = 13/36$ and the lattice size is $N = 900$. Solid lines are guides to the eye. Inset: maximum value of the structure factor $S_{\max}/N$ as a function of $1/\sqrt{N}$ for $\rho = 13/36$, $V/t = 5.4$ and $T/t = 1/12$; the dashed line is a linear fit for the three largest system sizes.

the SG into an insulating G. The latter is characterized by a finite value of $\widetilde{q}_{EA}$ and $\rho_s \simeq S(\boldsymbol{k}) = 0$ (i.e., $V/t \gtrsim 6.2$ in the figure). Within this glass phase quantum effects are largely suppressed. While glasses are well known to appear in disordered spin models, as well as in certain polydispersed systems of particles [106], here I demonstrate that glassy physics may emerge in a simple and rather general model of immediate experimental interest for bosons on a regular lattice.

The computed phase diagram of (3.1) is shown in **Figure 3.2** for a choice of particle density $\rho = 13/36$ as a function of $T/t$ and $V/t$.

At high temperatures I find a normal liquid (L) phase independently of the values of $V/t$, as expected. For sufficiently small interaction strength $V/t \lesssim 4.8$, this normal phase turns into a homogeneous superfluid by decreasing $T/t$, via a phase transition which is consistent with the Berezinskii-Kosterlitz-Thouless scenario. On the other hand, for large enough $V/t$ and following a quench to low $T$ the system displays a marked insulating glassy behavior with $\widetilde{q}_{EA} \neq 0$, $S(\boldsymbol{k}) = \rho_s = 0$ (panel (a) in **Figure 3.3** and full symbols in the corresponding inset). The interplay between glassy physics and superfluidity is mostly evident for values of $T/t$ below the dotted lines in **Figure 3.2**, resulting in the SG scenario discussed above.

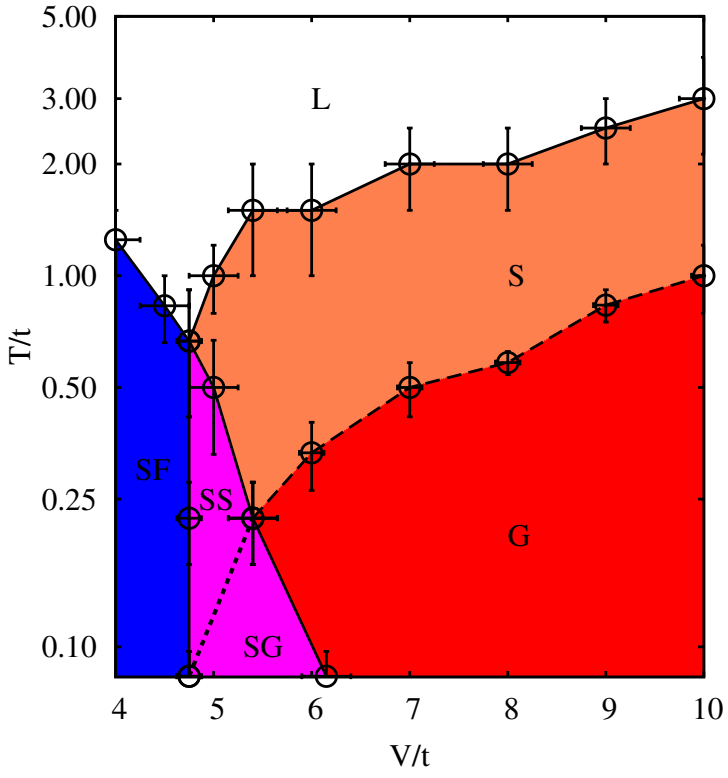


**Figure 3.2:** Phase diagram of model (3.1) with $r_c = 2$ as a function of temperature $T/t$ and interaction strength $V/t$, for particle density $\rho = 13/36$. Equilibrium phases: normal liquid (L), superfluid (SF), stripe-crystal (S), and supersolid (SS). A temperature quench to final values of $T/t$ below the dashed line leads to a glass (G). The existence of a superglass (SG) is demonstrated below the dotted line using the same quench protocol.

Interestingly, we find that thermal fluctuations can restore crystalline order for sufficiently large $T$. This is shown for intermediate temperatures in **Figure 3.2**, where a S (SS) phase intervenes between the low-temperature G (SG) and the high-temperature normal L. Here, the crystal is a floating stripe solid, with finite diagonal long range order in the thermodynamic limit. Examples for the finite size scaling of the maximum value of the structure factor $S_{\max}/N$ in the S and G phases are shown in the inset of panel (a) of **Figure 3.3** (empty and full symbols, respectively). While in the S phase $S_{\max}/N$ is essentially independent of the system sizes investigated in my study, in the G phase $S_{\max}/N$ vanishes in the thermodynamic limit. In both phases $\rho_s \simeq 0$.

The difference between the glassy and crystalline phases is shown in panel (c) of **Figure 3.3**, where I plot the maximum value of the structure factor $S^{(R)}_{\max}/N$ for each individual realization of a temperature quench at a given $V/t$ and final $T/t$. In the crystalline phases, $S^{(R)}_{\max}/N$ is essentially identical in all realizations and $S_{\max}/N$ remains finite in the thermodynamic limit. However, within the glassy phases, $S^{(R)}_{\max}/N$ can fluctuate widely and in average decreases to zero with the system size. As shown in panel (b) of **Figure 3.3** the dependence of $S^{(R)}_{\max}/N$ on the realization for the SG and the SS phase is similar to that for the G and the S ones, respectively.

Further insight into the phases of Hamiltonian (3.1) is given by the analysis of the averaged site-density maps in **Figure 3.4**. Specifically, I show results for a portion of the system and for a choice of $T/t$ and $V/t$ such that the system is a SF [panel (a)], a SG [panel (b)], and a G [panels (c-e)]. For comparison, panel (f) shows a cluster-type crystalline phase (i.e., $S(\boldsymbol{k}) \neq 0$) stabilizable at a density $\rho = 1/3$, for $V/t = 10$ and $T/t = 1$. In the homogeneous SF the average occupation number at each site equals the density $\rho$ of the system, as expected. The resulting value of $\widetilde{q}_{EA}$ is thus negligible. Conversely, when $V/t$ is large [panel (c)] the spatial density is highly inhomogeneous: particles form self-assembled clusters characterized by different numbers of constituents and spatial orientations, as well as by varying inter-cluster distances. These features lead, in the thermodynamic limit, to the absence of diagonal long

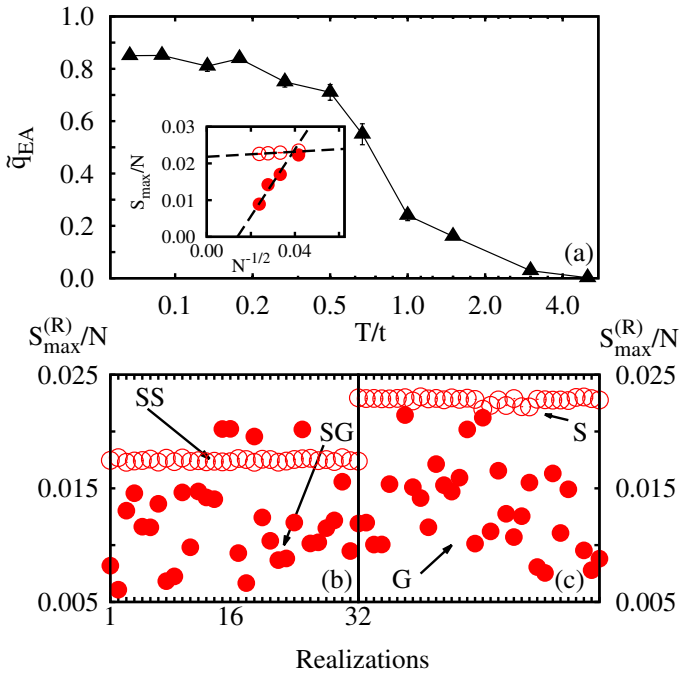


**Figure 3.3:** (a): Normalized Edwards-Anderson order parameter $\widetilde{q}_{EA}$ for model (3.1) as a function of $T/t$ for $V/t = 10$, $N = 900$ and $\rho = 13/36$. The solid line is a guide to the eye. Inset: Size dependence of $S_{\max}/N$ for $V/t = 10$. $T/t = 1/12$ and $T/t = 3/2$ for full and empty symbols, respectively. Dashed lines are fits to numerical data. (b-c): Maximum value of the structure factor $S^{(R)}_{\max}/N$ obtained in a given realization of a quench, plotted as a function of the number of different quench realizations. The latter only differ in the (random) initial condition and in the thermalization seed. The corresponding phases in the thermodynamic limit are indicated. Fluctuations in the values of $S^{(R)}_{\max}/N$ indicate glassy behavior. The parameters are: $N = 1764$, $T/t = 1/2.5$, $V/t = 5$ (SS), $N = 2304$, $T/t = 1/9$, $V/t = 5.4$ (SG), $N = 1296$, $T/t = 1/0.7$, $V/t = 10$ (S), $N = 1296$, $T/t = 1/12$, $V/t = 10$ (G).

range order, similarly to an (emergent) polydispersity. Noticeably, the occupation number of lattice sites between clusters is here substantially suppressed, signaling particle localization. The resulting glass phase is insulating, similarly to, e.g, a regular Bose glass obtained by externally induced disorder [85].

Panel (b) shows that cluster formation and inhomogeneity persists even at intermediate values of $V/t$, leading to a nonzero value of $\widetilde{q}_{EA}$ in

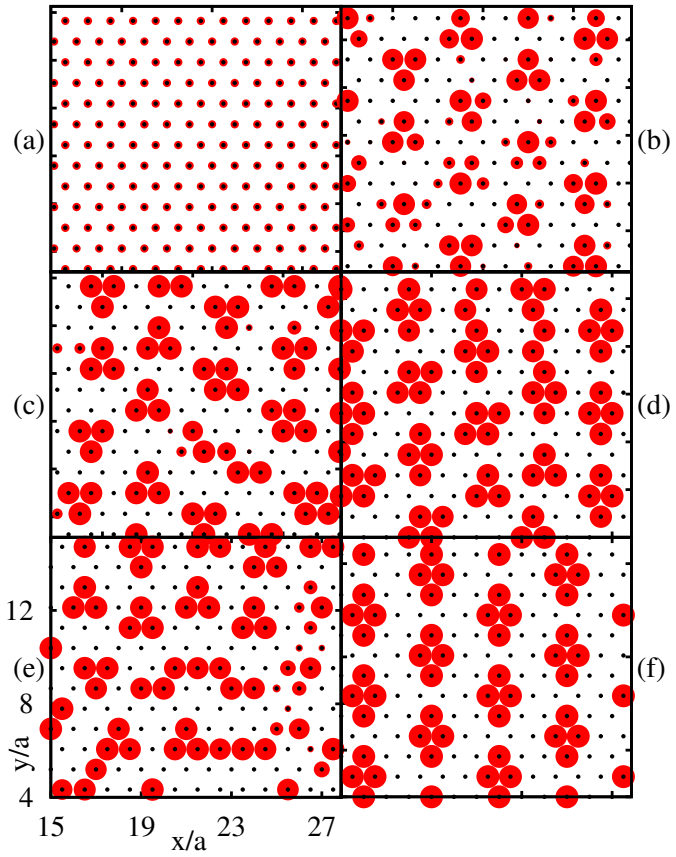


**Figure 3.4:** Averaged site density for a portion of the system. Black circles depict the lattice sites. Density values are proportional to the size of red circles. Panel (a) shows an homogeneous superfluid phase ($T/t = 1/9$ and $V/t = 4$); panels (b) and (c), refer to a SG ($T/t = 1/12$, $V/t = 5.4$), and to a normal G ($T/t = 1/12$, $V/t = 10$), respectively. In panels (a-c) the density is $\rho = 13/36$. Panels (d) and (e) show the glassy density map obtained for $\rho = 0.401$ ($V/t = 10$, $T/t = 1/12$), and for the same density of panels (a-c), using the purely repulsive potential (1.2) with $V_0/t = 30$, $T/t = 1/3$, respectively. Panel (f): a crystalline structure stabilizable at $\rho = 1/3$, $V/t = 10$ and $T/t = 1$.

the absence of crystalline order. The occupation of inter-cluster lattice sites is here enhanced with respect to panel (c). Such an enhancement is due to the presence of quantum fluctuations and exchanges of identical particles, responsible for the finite value of $\rho_s$ and thus of superglassiness.

While the main focus of this study is the Hamiltonian (3.1) with

$r_c = 2$ and $\rho = 13/36$, in the following I discuss the dependence of the observed glassy behavior on the radius $r_c$ of the interaction potential of Hamiltonian (3.1), on the particle density $\rho$ satisfying the clusterization condition and on the details of the cluster-forming potential and of the quenching protocol. I also investigate the relation between the appearance of glassiness and cluster formation.

- Panel (a) of **Figure 3.5** shows results for the maximum value of the structure factor $S^{(R)}_{\max}/N$ for different realizations of a low-temperature quench for interaction radius $r_c = 3$ (larger than that above) with particle density $\rho = 13/36$ (same as above). The interaction strength is chosen $V/t = 10$, the temperature $T/t = 1/12$, and the system size $N = 1296$. I find that, despite the relatively small value of $N$, $S^{(R)}_{\max}/N$ clearly fluctuates between different realizations.

  In addition, panel (b) shows that the structure factor averaged over the individual realizations $S_{\max}/N$ vanishes in the thermodinamic limit. In the same limit, the superfluid fraction is $\rho_s \simeq 0$, while the (realization averaged) Edwards-Anderson parameter $\widetilde{q}_{EA}$ stays finite. These results demonstrate the existence of a glass phase with $r_c = 3$. Here I have utilized the same parameters of the glass phase for $r_c = 2$ in the phase diagram in **Figure 3.2**, showing that in this case an increase of $r_c$ does not alter the physical scenario.

- **Figure 3.6** shows values of the Edwards-Anderson parameter $\widetilde{q}^{(R)}_{EA}$ and $S^{(R)}_{\max}/N$ for different realizations of a temperature quench with target $T/t = 1/12$, $V/t = 5.4$, $r_c = 2$ and $\rho = 0.3650$. The latter corresponds to a variation at the percent level of the density value of **Figure 3.2** (i.e., $\rho = 13/36$). The system size is $N = 2304$.

  Also in this parameter regime the maximum value of the structure factor [panel (b)] depends on the quench realization, showing the same glassy behavior we observed at $\rho = 13/36$ [see panels (b-c) of **Figure 3.3**]. The fluctuations of $\widetilde{q}^{(R)}_{EA}$ are much less pronounced

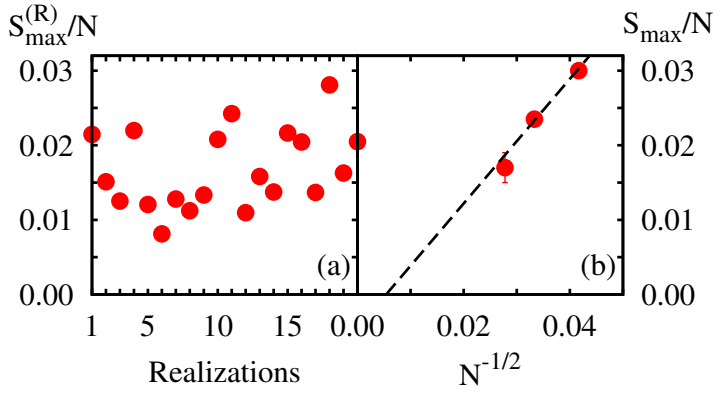


**Figure 3.5:** (a): Maximum value of the structure factor $S^{(R)}_{\max}/N$ for different realizations. The system size is $N = 1296$. (b): size dependence of the average structure factor $S_{\max}/N$. In both panels $\rho = 13/36$, $T/t = 1/12$ and $V/t = 10$. The Hamiltonian of the system is (3.1) with $r_c = 3$.

[panel (a)] and the values remains large. In addition, I find that here structural disorder and inhomogeneity coexist with finite superfluid fraction, demonstrating the existence of a superglass.

At sufficiently large $V/t$, the existence of glassy phases for the cluster-forming potential in (3.1) has also been verified for values of the particle density fulfilling the clusterization condition $r_c\sqrt{\rho} > 1$ as high as $\rho \simeq 0.4$. For this value of $\rho$, an example of structural disorder and cluster formation is given in panel (d) of **Figure 3.4**.

Given the results above, as (3.1) is particle-hole symmetric, one may expect that glass behavior could be observable for essentially all densities with $r_c\sqrt{\rho} > 1$, $r_c = 2$ and an appropriate choice of $V/t$.

- To underline how cluster formation plays a crucial role for the observation of the glassy scenarios investigated here, I show in **Figure 3.7** estimates of $\widetilde{q}^{(R)}_{EA}$ and $S^{(R)}_{\max}/N$ for different realizations of a temperature quench with target $T/t = 1/12$, $V/t = 10$, $N = 2304$ and $r_c = 1$. With this choice of parameters the interaction potential does not support clusterization and the equilibrium phase is a

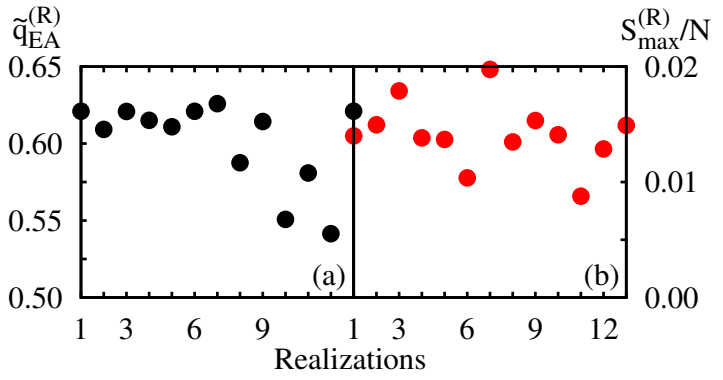


**Figure 3.6:** Edwards-Anderson parameter $\tilde{q}_{EA}^{(R)}$ (a) and maximum value of the structure factor $S_{\max}^{(R)}/N$ (b) for different realizations. The system size is $N = 2304$, $\rho = 0.3650$, $T/t = 1/12$ and $V/t = 5.4$. For these parameters and the density $\rho = 0.3611$ the system is a superglass in the thermodynamic limit (see **Figure 3.2**).

supersolid [88].

As shown in the figure, the values of $\tilde{q}_{EA}^{(R)}$ and $S_{\max}^{(R)}/N$ are essentially identical in all realizations, i.e., the quench is ineffective and the equilibrium physics is restored. Conversely, at the same temperature, for $r_c = 2$ and particle density satisfying the clusterization condition, I find that the quenched counterpart of a supersolid is a superglass (see **Figure 3.2**). This indicates that cluster formation enhances frustration in the system, favoring glassy behavior.

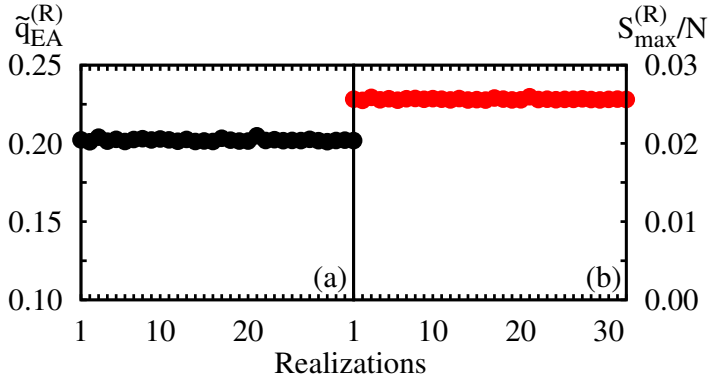


**Figure 3.7:** Same observables as in **Figure 3.6** for $T/t = 1/12$, $V/t = 10$, $N = 2304$ and $r_c = 1$.

- Since in experiments it should be easier to perform a quench in $V/t$ (which, e.g., with Rydberg atoms would entail modifying the laser parameters for Rydberg dressing, changing $V$, or for the depth of the confinement to the optical lattice, changing $t$) than in $T/t$, I have investigated whether the glassy behavior described above is also found upon a quench in the interaction strength.

  I find that similar behavior of $\widetilde{q}_{EA}^{(R)}$ and $S_{\max}^{(R)}/N$ to the one in the superglass and glass phases described above is obtained when, starting from a value at which the system is superfluid, $V/t$ is abruptly increased to an intermediate or large value (**Figure 3.8**). Following this simulation protocol at fixed (low enough) $T/t$ (i.e., a quench in $V/t$) I find no crystalline order and inhomogeneity in the thermodynamic limit. Specifically, the system is a superglass or a normal glass for intermediate or large values of $V/t$, respectively. This is entirely analogous to what found in the above results for a quench in $T$.

- I check that glassy phases similar to those described above can be obtained replacing the soft-shoulder interaction in (3.1) with the interparticle interaction between Rydberg-dressed atoms $V_{dd}(r)$ in (1.2), for interaction strength $V_0$ sufficiently large. As an example, panel (e) in **Figure 3.4** shows results for the density within the glass phase with $V_0/t = 30$.

I also study [54] the system described by the Hamiltonian (3.1) for $r_c = 2\sqrt{2}$ on a square lattice. I perform the calculations using my PIMC code with Worm updates, as well as an implementation of the Stochastic Green Function (SGF) algorithm [107]. The latter is a PIMC method with a different set of updates.

I consider sizes of up to $N = 48 \times 48$ and temperatures as low as $T/t = 1/20$. For given sets of system parameters, I run independent simulations to avoid possible effects of metastability due to the large low-energy degeneracy discussed above.

My simulations are performed at fixed density $\rho = 5/36$. I measure the superfluid fraction $\rho_s$ using the estimator (2.12) for $d = 2$, the

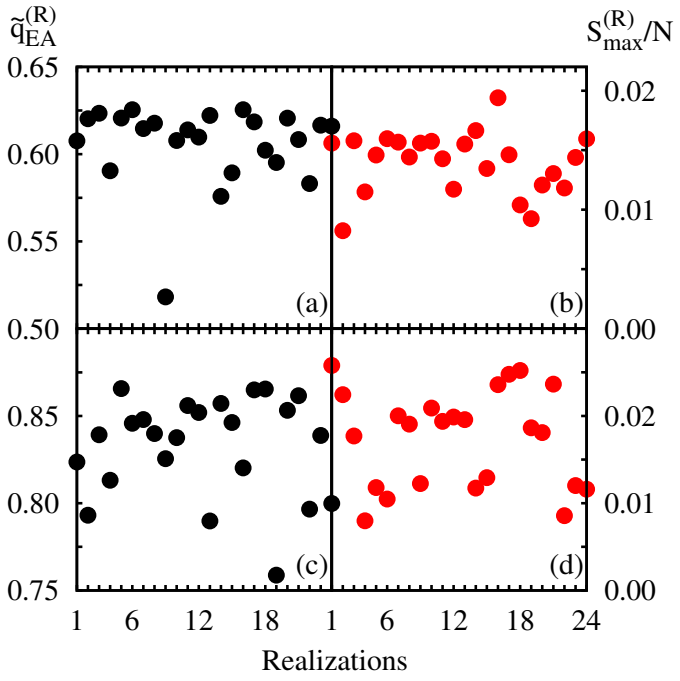


**Figure 3.8:** Same observables as in **Figure 3.6** when the simulation protocol is based on a quench in the interaction strength. Here $\rho = 13/36$, $N = 2304$ and $T = 1/12$. The final value of the interaction strength is $V/t = 5.4$ [panels (a) and (b)] and $V/t = 10$ [panels (c) and (d)]. In the thermodynamic limit the former choice of $V/t$ leads to a superglass, the latter, to a normal glass.

structure factor defined in (3.3), as well as the equal-time, site-averaged single-particle Green function (2.14), i.e.

$$G(\boldsymbol{r}) = -\lim_{\tau_2 \to \tau_1^+} \frac{1}{N} \sum_{i=1}^{N} \left\langle T_\tau \left( b_i(\tau_1) b_{i+\boldsymbol{r}}^\dagger(\tau_2) \right) \right\rangle \tag{3.5}$$

Initial results show that for small $V/t \lesssim 2.5$, the system equilibrates to a superfluid phase, while a SS phase is encountered for intermediate interaction strength (i.e., $2.5 \lesssim V/t \lesssim 4.5$). Example results for the behaviour of the order parameters $\rho_s$ and $S(\boldsymbol{k})$ are shown in **Figure 3.9**. In particular, panel (a) shows the dependence of $\rho_s$ on $V/t$ for $L = 36$ and $T/t = 1/20$. Here $\rho_s$ is shown to decrease monotonically from a constant finite value at $V/t \lesssim 2.5$ to zero at $V/t \gtrsim 4.5$. Panel (b) shows that for

$V/t = 4$ $S(\boldsymbol{k})$ has a finite, size-independent value, signaling crystalline order consistent with SS behaviour (green down-pointing triangles).

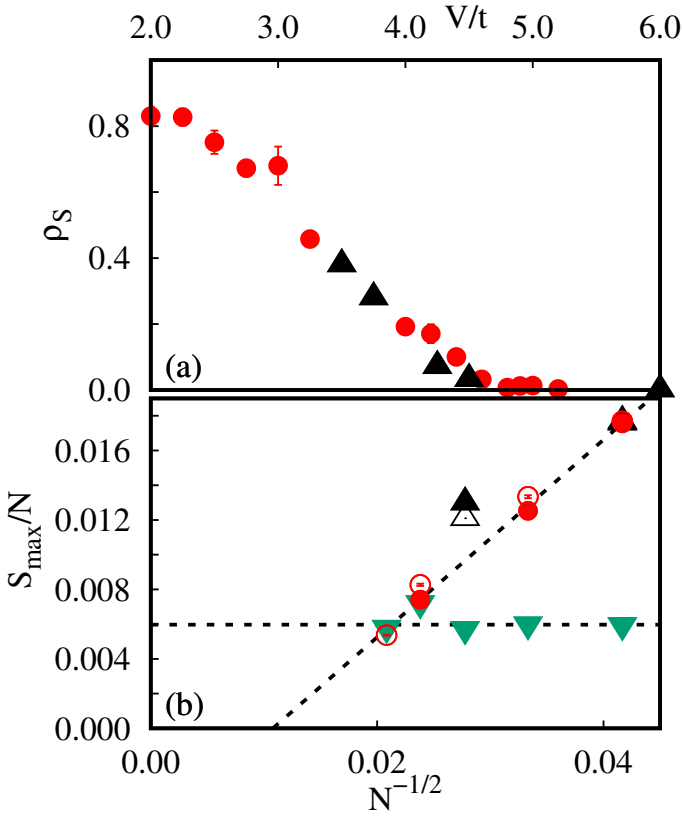


**Figure 3.9:** (a) Superfluid density $\rho_s$ as a function of $V/t$, for $\beta t = 20$ and $L = 36$. In panels (a) and (b), dots and triangles correspond to data obtained with the SGF and worm algorithms, respectively. (b) Maximal value of the static structure factor $S(\boldsymbol{k})$ as a function of $1/L$. Green down-pointing triangles: $V/t = 4$. Red dots and black up-pointing triangles: $V/t = 6$. Full and empty symbols denote $\beta t = 20$ and 4, respectively. Dashed lines are guides to the eye.

For $V/t = 6$ (black up triangles and red dots in **Figure 3.9**), $S(\boldsymbol{k})$ vanishes in the thermodynamic limit. This same behaviour is obtained for values of the interaction strength $V/t \gtrsim 4.5$. Therefore, I find a phase transition from a SS to a disordered, non superfluid phase. Surprisingly, we find that in the latter the Green function decays algebraically at long distances, as shown in **Figure 3.10**.

This unusual behavior is characteristic of an exotic phase known

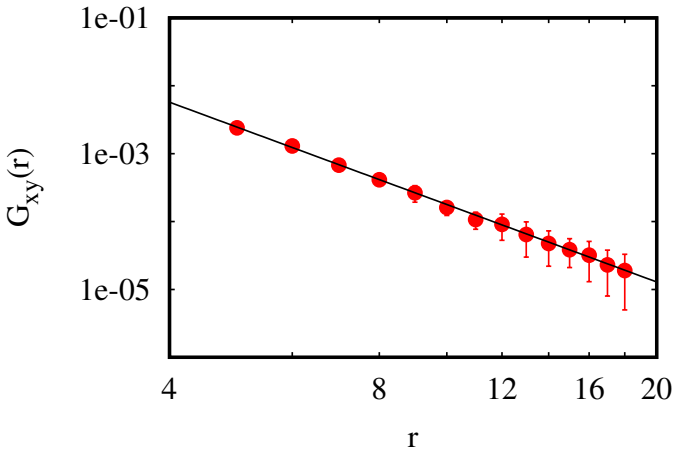


**Figure 3.10:** Green function $G_{xy}(|\boldsymbol{r}|)$, defined as (3.5) averaged over the $x$ and $y$ direction *vs* distance, for $V/t = 6$, $L = 36$, $\beta t = 20$ and density $\rho = 5/36$. The black continuous line is a fit to a power-law function $ar^{-b}$, with $a = 1.1(1)$ and $b = 3.79(6)$.

as *Bose Metal* [108, 109, 110, 111], a state describing conducting, yet non-superfluid bosons in two dimensions. Calculations at very large system sizes (up to $N = 96 \times 96$) and very low temperatures (down to $T/t = 1/96$) are currently running, to investigate possible temperature and size dependences of the aforementioned physical picture.

In conclusion, I demonstrate that glassy phases can be realized for a broad class of simple bosonic, frustration-free Hamiltonians of the extended Bose-Hubbard type. For intermediate interaction strength the interplay between quantum fluctuations, statistics and glassy physics gives rise to an exotic SG scenario, where glassiness coexists with superfluidity, in contrast to a conventional Bose glass. In the model studied by me, frustration arises from the self-assembling of clusters, which is a direct consequence of the (isotropic) inter-particle interaction potential at high enough density.

I also study the model (3.1) with $r_c = 2\sqrt{2}$ on a square lattice, up to system sizes of $N = 48 \times 48$ and temperatures $T/t = 1/20$. Preliminary results show in this parameter range a phase transition between a SS and an intriguing disordered and non-superfluid phase. The nature of this phase transition is under investigation, via large-scale and low-

temperature simulations, to understand if, e.g., structural order and superfluidity disappear at the same time or if an intermediate phase is present, and to investigate possible temperature and size dependences of the aforementioned physical picture.

The physics described in my study should be directly relevant for experiments with ultracold Rydberg-dressed atoms in optical lattices (see section 1.3). I hope that my results will provide new insights for unveiling mechanisms for frustration-induced phenomena.

## 3.2 Variational Studies of the $t-J$ Model with two holes

The theoretical investigation of the ground state properties of strongly correlated systems is one of the hardest problems in condensed matter physics. Many relevant models lack an analytical solution, and the exact diagonalization (ED) of the Hamiltonian matrix, while certainly offering useful insights, remains restricted to system sizes in general too small to provide a reliable description of the physical scenarios in the thermodynamic limit. In order to overcome this limitation a variety of numerical techniques have been developed, each of which has an optimal realm of applicability. For example, PIMC methods, as well as other QMC approaches [112] provide essentially exact results for unfrustrated bosonic problems in any spatial dimension. However, as previously mentioned, QMC is hardly applicable without approximations to frustrated bosonic or fermionic systems, where the sign problem results in an exponential loss of accuracy of the results when decreasing temperature or increasing the number of particles [20]. Conversely, variational approaches based on the optimization of a trial wavefunction (WF) are sign-problem free; however, their accuracy ultimately depends on the choice and flexibility of the adopted ansatz for the WF. Recently, impressive effort has been devoted to the development of tensor-network WF's able to describe strongly correlated systems in two spatial dimensions (2D: see, e.g., [113] for a review) i.e., where the applicability of Matrix Product States [114, 115, 116, 117] and Density Matrix Renormalization Group [118] methods, extremely accurate in 1D, appears problematic.

One of the fundamental models used to characterize the behavior of strongly correlated electrons in 2D is the $t-J$ model, which is thought to provide an effective Hamiltonian description of the basic features of superconducting copper oxides. Key properties of the insulating copper-oxide planes at half-filling are reproduced by the spin-$1/2$ antiferromagnetic Heisenberg model i.e., the limiting case of the $t-J$ Hamiltonian in the absence of holes [19]. The presence of mobile holes that may change

the nature of the copper-oxide planes from insulating to superconducting is described in the $t-J$ model via an additional nearest-neighbor hopping term. The resulting Hamiltonian reads

$$\widehat{H} = -t \sum_{\{i,j\},\sigma} \left( \widehat{C}^{\dagger}_{i\sigma} \widehat{C}_{j\sigma} + \text{h.c.} \right) + J \sum_{\{i,j\}} \left( \widehat{\boldsymbol{S}}_i \cdot \widehat{\boldsymbol{S}}_j - \frac{\widehat{n}_i \widehat{n}_j}{4} \right) \tag{3.6}$$

$\widehat{C}_{i\sigma}$ is the annihilation operator for a spin-$1/2$ fermion with spin component $\sigma$ on the site $i$, $\widehat{\boldsymbol{S}}_i$ is a shorthand notation for the spin projection operators on site $i$, i.e. $\widehat{\boldsymbol{S}}_i = \left( \widehat{\boldsymbol{S}}^x_i, \widehat{\boldsymbol{S}}^y_i, \widehat{\boldsymbol{S}}^z_i \right)$, and $\widehat{n}_i = \sum_\sigma \widehat{C}^{\dagger}_{\sigma i} \widehat{C}_{\sigma i}$, $\{i,j\}$ denotes sum over nearest-neighbor sites, and double occupancy of lattice sites is forbidden. In (3.6), $J > 0$ is the antiferromagnetic coupling, and $t > 0$ the hopping amplitude, taken in the following as energy unit. The lattice spacing is taken as length unit.

Aside from its physical interest related to its possible direct relevance to high-temperature superconductivity, the model Hamiltonian in (3.6) constitutes one of the most challenging benchmarks to assess the accuracy of a given variational approach/WF. For this problem "exact" QMC techniques are applicable at half-filling [119], where the $t-J$ model does not have fermionic character, as well as to the static single-hole scenario. Accurate QMC strategies are also possible in the case of a single mobile hole [120]. The addition of a second hole, however, introduces a severe sign problem that calls, in the QMC framework, for various, hardly controllable approximations and workarounds. A valid option to tackle the two-hole problem in (quasi-) 1D ladder geometries is DMRG [121] while in 2D the optimization of a suitable WF that allows for the investigation of system sizes larger than those treatable with ED likely represents a preferable choice. In this framework the estimated ground state energy, as a strict upper bound of the actual value, constitutes a natural figure of merit to evaluate the accuracy of different ansatze.

In my work [21] I study the ground state of two holes in the $t-J$ model by using the VMC approach with the EPS wavefunction, described in section 2.3. As previously mentioned, this ansatz has been

successfully employed to investigate different unfrustrated and frustrated models providing results of comparable or better accuracy than those obtainable with alternative WF's or techniques [69, 70, 71, 72].

In the case of a single mobile hole [72], for example, it provides estimates of ground state energy and hole spectral weight in excellent agreement with the most accurate results available in literature, based on QMC [120]. Here, I show that an EPS WF including both square and linear plaquettes of limited sizes is able to faithfully describe the ground state of two holes in the $t-J$ model. The error on the obtained estimates of the ground state energies for (3.6) relative to the exact ones available for the $N = 4 \times 4$ lattice is of the order or less than $0.1\%$ for all values of $J/t$ explored in this work. By considering square lattices of much larger size (i.e., up to $N = 256$) I show that binding of the two holes occurs for all of the analyzed values of $J/t$; specifically, I find an exponential decay of the probability of finding two holes at distance $r$ in the large-$r$ limit and that the two-hole binding energy, although with an absolute value considerably smaller than the one of the system with $N = 16$, stays negative in the thermodynamic limit. I estimate $J_c/t \simeq 0.19$ as the critical value below which the existence of a bound state characterized by the $d_{x^2-y^2}$ symmetry, predicted by previous studies in the chosen parameter range, is excluded.

The accuracy of the presented findings for the two-hole $t-J$ model is a fundamental step towards the design of an EPS WF for the finite hole concentration scenario where the physics is still not completely understood. It is worth mentioning that relevant states proposed for the many-hole problem have a straightforward representation in terms of EPS [122] and essentially every WF may systematically be improved by taking advantage of the peculiar characteristics of the EPS ansatz.

The adopted wavefunction for the study of the $t-J$ model is the EPS ansatz, introduced in section 2.3, with plaquettes of two different types: along with simple square ones, linear plaquettes connecting the positions of the two holes are also employed. The considered size for the plaquettes of both types is 9 sites. I carry out independent optimizations of the state in (3.6) for each lattice size and value of $J/t$ considered

here via the VMC algorithm described in section 2.3, and I use the same numerical approach to estimate the observables of my interest. In particular, for $0.4 \leq J/t \leq 2.0$, I compute:

- The *two-hole ground state energy* $\delta E_2/t = (E_2 - E_0)/t$, where $E_2$ ($E_0$) is the ground state energy obtained for the Hamiltonian (3.6) in the presence of two holes (at half-filling).
- The probability distribution $P(r) = \sum_{i<j} \delta(r_{ij} - r)\widehat{n}_i^h \widehat{n}_j^h$ of finding the two holes at a distance $r$, where $\widehat{n}_i^h$ is the number of holes on the site $i$.
- The *two-hole binding energy* $\Delta/t = \delta E_2/t - 2\delta E_1/t$, where $\delta E_1/t = (E_1 - E_0)/t$ is the difference between the one-hole ground state energy of (3.6), obtained by VMC calculations with the EPS ansatz with $3 \times 3$ square plaquettes [72], and the aforementioned half-filling ground state energy.

It has to be stressed that with 9-site plaquettes I obtain remarkable agreement with ED calculations [123, 124, 125] for both the single- and the two-hole problems; similarly, on large lattices the computed estimates of both the single- and the two-holes ground state energies are in extremely good agreement with the most accurate results available in literature [120, 55] (see below). This is an important point, since a consistent increase of the plaquette size e.g., by considering square plaquettes of 16 sites would be extremely expensive from a computational point of view due to the dimension (i.e., 3) of the local Hilbert space of the $t-J$ model. My findings for $P(r)$ obtained for lattices of up to $N = 256$ sites, that is, much larger than those treatable with exact methods, demonstrate the existence of a two-hole bound state for any value of $J/t$ considered here. Estimates of the two-hole binding energy extrapolated to the thermodynamic limit and for values of $J/t$ lower than $0.4$ suggest that a two-hole bound state does not exist with the same symmetry characteristic of the range of $J/t$ values explored in my work for $J/t \lesssim 0.19$.

While for small system sizes (i.e., up to $N \simeq 16$) it is possible to describe the ground state properties of model (3.6) essentially exactly by means of an EPS WF based on a single plaquette that correlates all the lattice sites, such a choice is not a viable option for larger lattices. My EPS variational state with plaquettes comprising a limited number of sites provides accurate energy upper bounds for the lattice with $N = 16$ and is applicable to considerably larger lattice sizes using standard computational resources. For example, on the $4 \times 4$ square lattice I find, at $J/t = 1.0$, $E_2 = -18.8007(1)t$ which compares extremely well with the exact result [123] $E_2^{ex} = -18.8061t$. The resulting EPS two-hole ground state energy is $\delta E_2/t(J/t = 1.0) = 0.4246(1)$, which has to be compared with $\delta E_2^{ex}/t(J/t = 1.0) = 0.4223$.

It is interesting to contrast my results with those obtained by means of a Green's function Monte Carlo (GFMC) approach based on the extrapolation of transient energy estimates generated by the GFMC algorithm starting from a suitable initial state. For the two-hole $t-J$ model, the GFMC technique is affected by the fermionic sign problem and the mentioned extrapolation can be performed by using just a few transient estimates before the occurrence of an uncontrolled growth of the statistical uncertainty ultimately due to sign instability. Consequently, the choice of the initial state is crucial in the case of GFMC as it has to produce reliable estimates in a limited number of algorithm iterations. Although for $J/t = 1.0$ this procedure gives an extrapolated value $\delta E_2^{GFMC}/t(J/t = 1.0) = 0.42(1)$, in agreement with the EPS result, I remark that the GFMC zero-th, variational, iteration based on the initial WF provides a two-hole ground state energy more than $3$ times larger. This demonstrates that the EPS ansatz is much more accurate than the initial variational state adopted in [55] and, more importantly, suggests my WF as a nearly optimal one to start a GFMC numerical scheme consisting of few iterations. The latter, aside from the above mentioned possibility of adding variational flexibility to a general EPS WF by including larger plaquettes, constitutes a further opportunity to improve numerical estimates.

**Figure 3.11** shows EPS results for the two-hole ground state en-

ergy $\delta E_2/t$ as a function of the system size $N$ and various values of $J/t$. The relative error of my numerical estimates with respect to the exact results obtainable for the $N = 16$ lattice (i.e., the smallest considered here) is of the order of $0.5\%$ or less regardless of the $J/t$ value. On larger lattices my two-hole ground state energies compare extremely well with GFMC ones; at $J/t = 1.0$, for example, the estimated value for the $8 \times 8$ system is $0.238(2)$, in numerical agreement, taking into account the quoted error bars, with the GFMC result i.e., $0.26(2)$ [55]. By means of a simple extrapolation of my data to the thermodynamic limit based on a polynomial expansion in powers of $1/N$ (dashed lines in figures) I find that the two-hole ground state energy monotonically decreases with decreasing $J/t$ being e.g., $\delta E_2^{N=\infty}/t(J/t = 1.0) \simeq 0.185$ and $\delta E_2^{N=\infty}/t(J/t = 0.4) \simeq -3.05$. My extrapolated results are in substantial agreement with the estimates for the largest lattice size studied in this work (i.e., $N = 256$) pointing out how the EPS ansatz allows, for the model of my interest, to investigate lattices large enough to provide a good approximation of the physics emerging in the thermodynamic limit.

The probability $P(r)$ of finding the two holes at distance $r$ on the $4 \times 4$ lattice for chosen values of $J/t = 2.0$ and $0.4$ is plotted in the inset of **Figure 3.11**. This quantity displays an oscillating behavior with a global maximum at $r = 1$ for $J/t = 2.0$. For lower $J/t$ the position of such a maximum shifts to $r = \sqrt{2}$ and $P(r)$ at larger $r$ increases, signaling an enhanced propensity of the two holes to reside on distant lattice sites. This may possibly result for larger system sizes in an "unbound" two-hole ground state. Conversely, if the two holes form a bound state $P(r)$ is expected to feature an exponential decay at large distances (see, e.g., [126]).

**Figure 3.12** shows estimates of $P(r)$ on a lattice of $N = 64$ sites. Although the qualitative behavior of the two-hole distribution function is similar to that found for $N = 16$ here, as expected, holes are more separated on average. The smaller is the value of $J/t$, the larger is their tendency to increase their relative distance. However, for large $r$ my data are well described by the simple functional form $P(r) \sim e^{-r/\xi}$

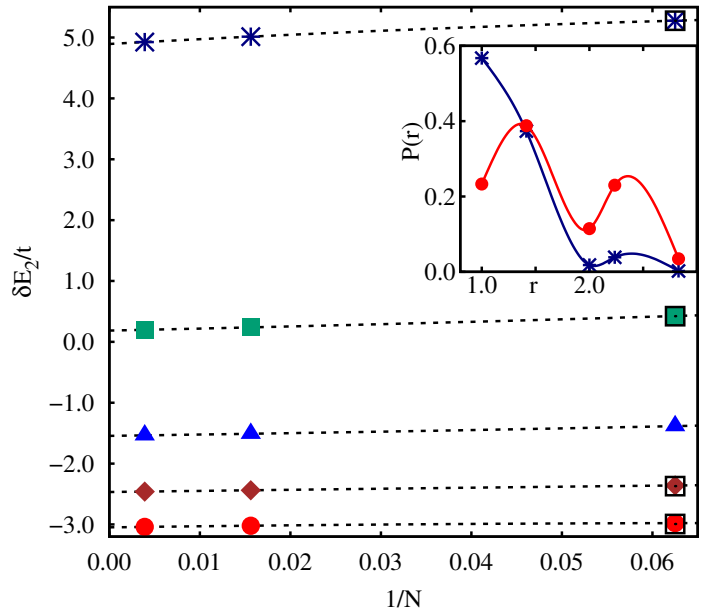


**Figure 3.11:** Two-hole ground state energy $\delta E_2/t$ as a function of the lattice size $N$. Values of $J/t$ are $2.0$ (stars), $1.0$ (squares), $1/1.5$ (triangles), $0.5$ (diamonds) and $0.4$ (circles). Error bars are smaller than the symbol size. Exact results [123, 124] available for the $4\times4$ lattice are also shown (empty squares) for comparison. The dotted lines are polynomial fitting functions in $1/N$ for the numerical data. Inset: Two-hole distribution function $P(r)$ for the $4\times4$ lattice; same symbols correspond to the same values of $J/t$ in the main panel, solid lines are guides to the eye.

where, for $J/t = 0.4$ (see inset), I estimate $\xi \sim 0.4$. By increasing the lattice size to $N = 256$ the value of $\xi$ stays essentially unchanged. On the basis of this analysis I can conclude that the two holes form a bound state for all the values $0.4 \leq J/t \leq 2.0$ examined in my study.

Quantitative information about the two-hole bound state are obtainable by computing the binding energy $\Delta/t$ defined above. A negative value of this quantity signals the existence of the bound state. In order to estimate $\Delta/t$, both the two- and the single-hole ground state energies are needed. The single-hole ground state energy is plotted as a function of the system size in **Figure 3.13**, for several values of $J/t$. The binding energy resulting from the combination of data in **Figure 3.11** and **Figure 3.13** displays a marked dependence on the system

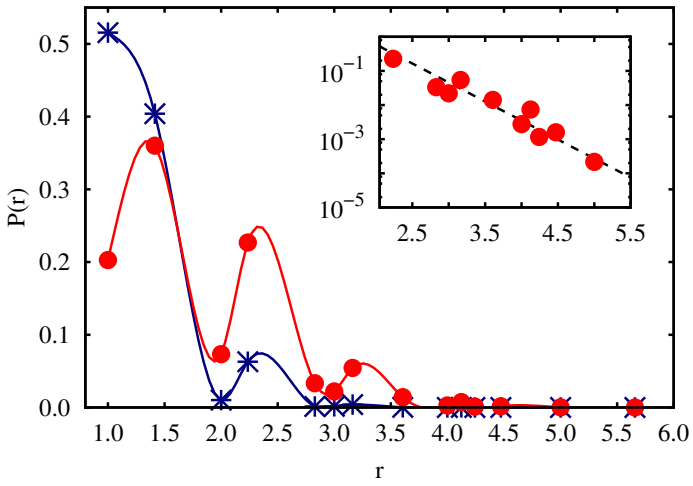


**Figure 3.12:** Two-hole distribution function on the $8 \times 8$ lattice. Values of $J/t$ are $2.0$ (stars) and $0.4$ (circles). Error bars are smaller than the symbol size; solid lines are guides to the eye. Inset: large distance decay of $P(r)$ for $J/t = 0.4$; the dashed line is the exponential fitting function adopted to describe the numerical data.

size as well as on the values of $J/t$. For example, for $N = 256$ I find $\Delta/t(J/t = 0.4) = -0.111(3)$, a value in agreement with the GFMC estimate of $-0.12(4)$, approximately $3$ times higher than that for the $4 \times 4$ lattice. On the other hand, on a $16 \times 16$ lattice when $J/t$ increases from $0.4$ to $1.0$, the two-hole binding energy decreases down to $\sim -0.39$.

Values of the binding energy extrapolated to the thermodynamic limit are plotted in **Figure 3.14**. Specifically, for each value of $J/t$, $\Delta^{\infty}/t = \delta E_2^{\infty}/t - 2\delta E_1^{\infty}/t$ is computed via the corresponding extrapolations of the two- and single-hole ground state energies (see dashed lines in **Figure 3.11** and **Figure 3.13**, respectively). By assuming, as in [55], the functional dependence

$$\frac{t}{J} = \frac{t}{J_c}\left[1 - \lambda \frac{\Delta^{\infty}}{t} \ln\left(\frac{\Delta^{\infty}}{t} \cdot \frac{1}{\epsilon}\right)\right] \tag{3.7}$$

I estimate the critical value $J_c \simeq 0.19t$ at which the two-hole binding energy extrapolated to the thermodynamic limit reaches zero. This estimate, in agreement with that obtained in the case of the $16 \times 16$ lattice, indicates that for $J \lesssim J_c$ a bound state of two holes, if present, is

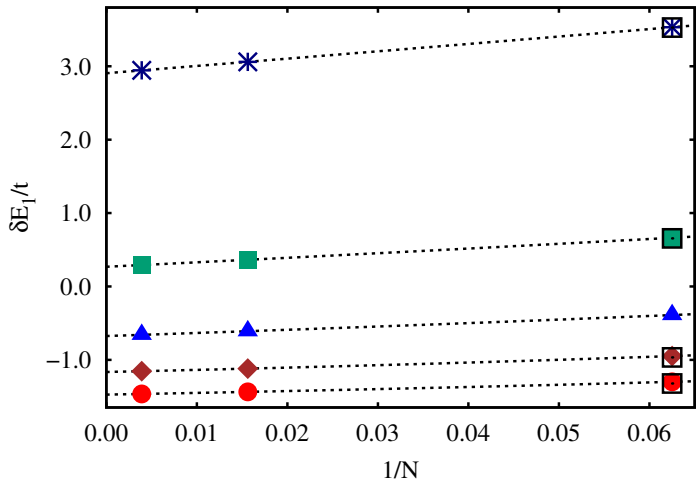


**Figure 3.13:** Single-hole ground state energy $\delta E_1/t$ as a function of the lattice size $N$. Estimates are obtained with the EPS ansatz used in [72]. Values of $J/t$ are $2.0$ (stars), $1.0$ (squares), $1/1.5$ (triangles), $0.5$ (diamonds) and $0.4$ (circles). Error bars are smaller than the symbol size. The dotted lines are polynomial functions in $1/N$ used to fit the numerical data. Exact results available for the $4 \times 4$ lattice are also shown (empty squares) for comparison.

characterized by a symmetry different from that (i.e., $d$-wave) predicted by several studies in the parameter range of **Figure 3.14**. Indeed, a change in the symmetry of the bound state should occur for $J/t \lesssim 0.18$ [56] or (or $0.15$ [57]).

In conclusion, I have shown that the entangled-plaquette variational ansatz can be applied to study the ground state properties of two mobile holes in a two-dimensional quantum antiferromagnet for lattice sizes considerably larger than those treatable with exact approaches. Obtained energy estimates are in remarkable agreement with exact results on a $N = 16$ lattice. I have extended my analysis to a maximum system size of $N = 256$, demonstrating the existence of a two-hole bound state for all the values of $J/t$ explored here. An extrapolation of my estimated two-hole binding energy in the large $N$ limit to low values of $J/t$ results in a critical $J_c \simeq 0.19t$ below which a bound state with d-wave symmetry is not expected. Including e.g., the $p$-wave symmetry in the EPS ansatz to investigate the existence of a different two-hole bound state in the ground state for $J/t \lesssim 0.19$, as well as studying the

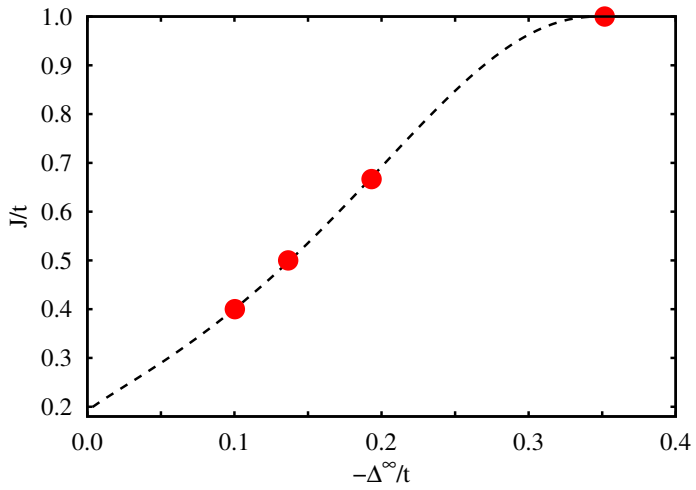


**Figure 3.14:** $J/t$ versus opposite binding energy extrapolated to the thermodynamic limit $-\Delta^{\infty}/t$. The dashed line is a fit to the numerical data using the function (3.7).

dependence of the physical properties discussed here on the presence of a next-nearest-neighbor hopping term in (3.6), are possible interesting extensions of my work.

Furthermore, although specific QMC approaches can still be adopted for the two-hole $t-J$ model at the price of a large error bar on the resulting estimates, in the finite hole density scenario, where the physical picture remains under debate [58, 59, 60], their applicability is unfeasible due to an even heavier sign problem. In such a case the EPS ansatz, in the framework of a simple, by definition sign-problem free, variational approach (e.g., the one employed here) may constitute a viable option either via a generalization of the WF employed here or as a systematic route to improve other relevant wave functions.

# Chapter 4

# Diagrammatic Monte Carlo

*This chapter is devoted to my work on the Diagrammatic Monte Carlo technique. After a quick overview of the method itself, I discuss the strategies chosen in my implementation of the algorithm, as well as possible future enhancements and applications for the latter.*

Diagrammatic Monte Carlo (DMC) techniques (see, e.g., [22] for a general introduction) are finite-temperature methods for the study of fermionic [127, 128, 129, 130, 63] and frustrated spin [61] systems. These approaches are unbiased, free from sign problems, and allow to study considerably large sizes at low temperatures. In the following, their theoretical framework will be illustrated, following the derivation in [131].

I will discuss the case of a spin-$1/2$ fermionic system in the grand-canonical ensemble, described by a Hamiltonian of the form $\widehat{K} = \widehat{K}_0 + \widehat{H}_1$, with

$$\widehat{K}_0 \equiv (-t) \sum_{\sigma} \sum_{\{i,j\}} \left( \widehat{C}^{\dagger}_{i\sigma} \widehat{C}_{j\sigma} + \text{h.c.} \right) - \mu \sum_{\sigma} \sum_{i} \widehat{n}_{i\sigma} \tag{4.1}$$

$$\widehat{H}_1 \equiv \sum_{\sigma\sigma'} \sum_{ij} V_{\sigma\sigma'}(x_i, x_j) \widehat{C}^{\dagger}_{i\sigma} \widehat{C}_{i\sigma} \widehat{C}^{\dagger}_{j\sigma'} \widehat{C}_{j\sigma'} \tag{4.2}$$

with the same definitions introduced in section 3.2 for the $t-J$ Hamiltonian (3.6). $\widehat{K}_0$ is therefore the noninteracting part, which can be solved exactly, while $\widehat{H}_1$ is a density-density interaction. In the following, $\langle\rangle_{\rm th}$ will denote the thermodynamical average with respect to the statistical density matrix of the system with Hamiltonian $\widehat{K}$, while $\langle\rangle_0$ will denote the average with respect to the noninteracting Hamiltonian $\widehat{K}_0$.

Without loss of generality, I will discuss a DMC algorithm sampling the diagrammatic expansion for the *finite-temperature single particle Green function*, the fermionic equivalent of (2.14), i.e.

$$G_{\alpha\beta}(z_1,z_2) = -\left\langle T_\tau\left(\widehat{C}_\alpha(z_1)\widehat{C}^\dagger_\beta(z_2)\right)\right\rangle_{\rm th} \tag{4.3}$$

where $\tau$ is the previously introduced imaginary time, $z\equiv(\boldsymbol{x},\tau)$ is a space-time coordinate, greek letters denote spin components, $T_\tau$ denotes time ordering in imaginary time, and time-dependent operators are defined via the *imaginary-time Heisenberg Picture*,

$$\widehat{O}(\boldsymbol{x},\tau) = e^{\widehat{K}\tau/\hbar}\widehat{O}(\boldsymbol{x})e^{-\widehat{K}\tau/\hbar}, \tag{4.4}$$

(4.3) can be used to compute many quantities of interest, such as, e.g., the thermodynamical mean values of energy and density. The standard interaction picture expansion in powers of the interaction Hamiltonian $\widehat{H}_1$ can be applied to rewrite the single particle Green function as

$$G_{\alpha\beta}(x,y) = -\frac{\sum_{n=0}^\infty (n!)^{-1}\int_0^\beta d\tau_1\ldots\int_0^\beta d\tau_n\left\langle T_\tau\left(\widehat{H}^I_1(\tau_1)\ldots\widehat{H}^I_1(\tau_n)\widehat{C}^I_\alpha(x)\widehat{C}^{I\dagger}_\beta(y)\right)\right\rangle_0}{\sum_{n=0}^\infty (n!)^{-1}\int_0^\beta d\tau_1\ldots\int_0^\beta d\tau_n\left\langle T_\tau\left(\widehat{H}^I_1(\tau_1)\ldots\widehat{H}^I_1(\tau_n)\right)\right\rangle_0}, \tag{4.5}$$

where the operators marked with $I$ evolve in imaginary time according to the *imaginary-time Interaction Picture*, i.e.

$$\widehat{O}^I(\boldsymbol{x},\tau) = e^{\widehat{K}_0\tau/\hbar}\widehat{O}(\boldsymbol{x})e^{-\widehat{K}_0\tau/\hbar} \tag{4.6}$$

Since $\widehat{H}_1$ is defined in (4.2) as a product of Fock operators $\widehat{C}$ and $\widehat{C}^\dagger$, any term of the series in (4.5) reduces to a thermal averages of time-ordered products of Fock operators, which have to be averaged on the statistical matrix of the noninteracting Hamiltonian.

The terms of the expansion (4.5) can be directly computed taking advantage of the *finite-temperature Wick theorem*. Ultimately, all contributions at a fixed order can be written in terms of the interaction function $V$ appearing in (4.2) and the Green function for the noninteracting system $G^0$, which can be computed exactly. Examples of first-order contributions to the numerator of (4.5) are

$$G^{(a)}_{\alpha\beta}(x,y) = \int dz_1 \int dz_2 \left( G^0_{\alpha\lambda}(x,z_1) G^0_{\lambda\beta}(z_1,y) G^0_{\mu\mu}(z_2,z_2) \mathcal{V}_{\lambda\mu}(z_1,z_2) \right) \tag{4.7}$$

$$G^{(b)}_{\alpha\beta}(x,y) = -\int dz_1 \int dz_2 \left( G^0_{\alpha\lambda}(x,z_1) G^0_{\lambda\mu}(z_1,z_2) G^0_{\mu\beta}(z_2,y) \mathcal{V}_{\lambda\mu}(z_1,z_2) \right) \tag{4.8}$$

$$G^{(c)}_{\alpha\beta}(x,y) = -\int dz_1 \int dz_2 \left( G^0_{\alpha\beta}(x,y) G^0_{\lambda\lambda}(z_1,z_1) G^0_{\mu\mu}(z_2,z_2) \mathcal{V}_{\lambda\mu}(z_1,z_2) \right) \tag{4.9}$$

Where $\int dz$ denotes an integration over imaginary time as well as a sum over the spatial coordinates. Here $\mathcal{V}(z_1,z_2) = V(x_1,x_2)\delta(\tau_1-\tau_2)$ is introduced to simplify the notation and equal-time Green function are to be interpreted as

$$G^0(\boldsymbol{x}_1,\tau,\boldsymbol{x}_2,\tau) = \lim_{\tau_2 \to \tau_1^+} G^0(\boldsymbol{x}_1,\tau_1,\boldsymbol{x}_2,\tau_2) \tag{4.10}$$

*Feynman diagrams* are a graphical tool which encodes information about the terms in the expansion (4.5) in a convenient representation. Each term in the series is biunivocally represented by a diagram, and rules exist to generate all diagrams for the terms of a given order, and to extract their contribution. For instance, diagrams (a), (b) and (c) in **Figure 4.1** correspond to (4.7), (4.8) and (4.9), respectively.

Dashed lines are referred to as *interaction lines*, and are associated

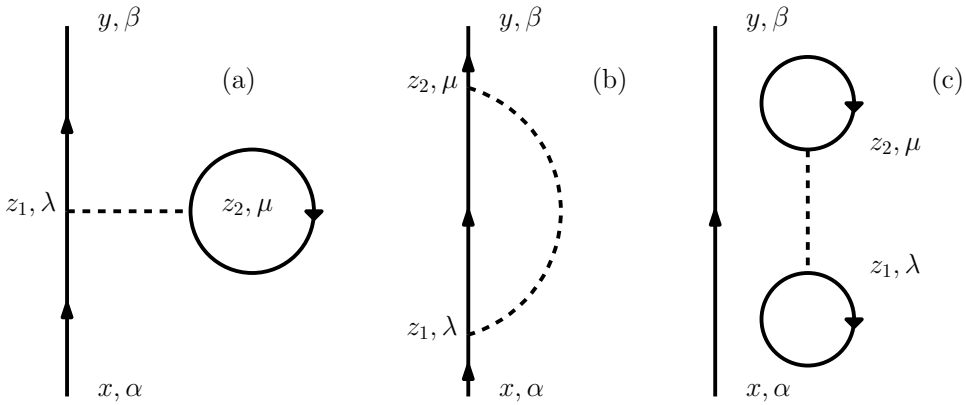


**Figure 4.1:** Feynman diagrams for the expressions in (4.7)-(4.9).

to interaction terms in the contribution, while straight lines are termed *particle lines*, and are associated to noninteracting Green functions $G^0$. Lines connect points known as *vertices*, each of which is associated with a space-time position and a spin component. Each vertex is touched by one interaction line and two particle lines, except for two of them which are only connected to a single particle line. These are called *external vertices*, and correspond to the coordinates and spin projections in which the interacting Green function is computed.

The diagrammatic representation allows an easier understanding and manipulation of the terms in the series. For instance, the effect of the denominator in (4.5) is to remove from the numerator all contributions from *disconnected* diagrams (i.e., those with subunits not connected with the rest of the diagram via lines). (4.5) therefore reduces to

$$G_{\alpha\beta}(x,y) = -\sum_{n=0}^{\infty}(n!)^{-1}\int_0^\beta d\tau_1 \ldots \int_0^\beta d\tau_n \left\langle T_\tau \left( \widehat{H}_1^I(\tau_1)\ldots\widehat{H}_n^I(\tau_n)\widehat{C}_\alpha^I(x)\widehat{C}_\beta^{I\dagger}(y)\right)\right\rangle_0^C \tag{4.11}$$

where the index $^C$ indicates that the sum is only restricted to connected contributions. At the first order in the series, for instance, the only diagrams to contribute are (a) and (b) in **Figure 4.1**, while diagrams like (c) are removed by the denominator. Determining which con-

tributions have to be summed is trivial in the diagrammatic formalism, allowing to considerably simplify the analysis.

Analysis of the perturbation series allows to find out the rules to draw all relevant $n$-th order diagrams for the imaginary-time Green function for the Hamiltonian given by (4.1) - (4.2):

- Draw all topologically distinct and connected diagrams containing $n$ interaction lines and $(2n+1)$ directed particle lines.
- Associate a factor $G^0_{\lambda\mu}(z_1, z_2)$ to any particle line running from the vertex of coordinates $z_1$ and spin $\lambda$ to the one of coordinates $z_2$ and spin $\mu$. Interpret any noninteracting Green function at equal times as in (4.10).
- Associate a factor $\mathcal{V}_{\lambda\mu}(z_1, z_2)$ to any interaction line connecting the vertices of coordinates $z_1$ and $z_2$ and spins $\lambda$ and $\mu$, respectively.
- Integrate over the space-time position of all internal vertices (as previously mentioned, these are the vertices which are touched by two particle lines and one interaction line, and are all but two of the vertices in the diagram).
- Sum over all repeating spin indices.
- Multiply each contribution by a factor $(-1)^n(-1)^F$, where $F$ is the number of fermionic loops (particle lines which close on themselves).

A similar rule scheme can be formulated for diagrams in momentum space in the case of translationally invariant Hamiltonians (instead of associating spatial coordinates to the vertices, each line carries a momentum). An important characteristic of the momentum space diagrammatic scheme, which will be of use later, is the conservation of momentum at each vertex (the sum of the momenta of incoming lines must balance the sum of the outgoing ones).

The use of rules such as these allows in principle to compute exactly the Green function for interacting systems. However, the number of

diagrams at order $n$ scales as $n!$, which prevents in practice analytical sums beyond a few orders.

DMC methods compute the sum over the diagrams via stochastic sampling: in particular, they employ a MH process where each diagram is weighted by the modulus of the contribution given to the Green function. Unlike in the PIMC case, the application of this modulus can be kept into account without causing numerical instabilities. The diagrammatic expansion of other quantities may also be sampled (for instance, many algorithms sample the *proper self-energy*, a quantity related to the Green function by relations known as *Dyson Equations*).

The MH process must allow to explore all possible values of the internal variables (positions and times of the vertices) as well as diagram topologies (the way the vertices are connected). Sampling both these quantities is a straightforward approach to ergodicity: this is however nontrivial, as changing the topology of the diagram usually requires complex and expensive nonlocal updates if any conservation laws, e.g. of momentum, have to be respected (even in real space, introducing fictitious line momenta and the relative conservation laws is sometimes useful, as will be explained below).

One possible way to perform an ergodic sampling is to use *worm-like updates* [22]. This scheme changes the topology of the diagram with simple local updates, by extending the configuration space to diagrams which violate the conservation laws.

In particular, one of the updates introduces two vertices in which momentum is not conserved, similar in role to the worm heads of the worm PIMC scheme introduced in section 2.2. Updates allow these heads to move along the lines and to swap (for instance) the lines which originate from them. The latter move allows to sample all topologies. Finally, an update may remove the unphysical vertices, reestablishing momentum conservation laws. The contribution to the Green function (or to other observables) is only measured in the physical configuration sector. Other, more trivial updates allow to move the vertices in time and space and to increase or decrease the order of the diagram.

*Bold Diagrammatic Monte Carlo* (BDMC) schemes [61, 63, 130] use

this kind of updates in conjunction with self-consistency techniques which aim to reduce the number of diagrams to sample. Depending on the actual self-consistency scheme, checks to avoid double-counting of diagrams have to be performed: the latter are considerably easier to execute in momentum space, or in real space with the inclusion of fictitious line momenta, justifying the necessity of updates which can take conservation laws into account. BDMC has been applied to study, e.g., frustrated spin systems [61] and fermionic systems like the 2D Hubbard model [63].

Another possible approach to sample diagram topologies is to use the *Determinant Diagrammatic Monte Carlo* (DDMC) scheme [128, 129]. In a nutshell, the algorithm only samples the space-time positions of the vertices: for a given set of the latter, the sum over all possible topologies with those vertex positions is computed exactly. This is accomplished via an alternative formulation of the Wick theorem, which allows to write the sum over all topologies (connected and disconnected) in a relatively easy to compute determinantal form (see, e.g., [132]).

This approach has the advantage of keeping into account exactly all cancellations from diagrams with opposite signs, which have to be sampled if using worm-like updates. Since the number of diagrams scales factorially with the diagram order, sampling becomes less and less efficient with respect to the determinantal approach for large orders. The latter allows therefore a considerably improved treatment of topologies.

Due to the presence of both connected and disconnected topologies in the sum resulting from the determinantal formalism, the most direct approach [128, 129] is to sample both the numerator and the denominator in (4.5), removing the disconnected contributions by performing the ratio. However, both the numerator and the denominator of (4.5) diverge in the thermodynamic limit: this implies that very long sampling times or approximations are required to have accurate results for large sizes.

A recently introduced improvement for the DDMC approach [62] allows to solve these issues by summing only connected contributions, eliminating the need to perform the ratio in (4.5). This is accomplished

by exploiting relations which link the sum of connected diagrams to the sum of both connected and disconnected contributions. The latter is still computed using the aforementioned determinantal formalism, and the relations are employed to remove from it all disconnected diagrams.

This improved approach (which will be denoted by IDDMC for the sake of clarity) allows to study sizes comparable to those reached via BDMC, while retaining the more accurate treatment of diagram topologies; the method has been successfully compared with BDMC [62] in the context of the 2D Hubbard model, yielding comparable result with much better accuracy. However, IDDMC suffers from some limitations: for instance, it is currently restricted to diagrams in coordinate space, and it does not allow the application of self-consistency techniques.

I have implemented a DMC code following the IDDMC approach. The latter was chosen for the aforementioned enhanced capability of sampling diagram topologies, as well as for the considerably simpler structure of the algorithm. My code is currently under testing, with many components already fully functioning as intended.

I included in my implementation the necessary instruments to treat both the case of on-site and of extended-range interactions. While relatively harder to implement, the latter offer the possibility to study several fermionic systems of interest (like, e.g., the fermionic counterpart of the bosonic lattice model studied in section 3.1).

A considerable amount of work is devoted in the DMC community to find new techniques to keep into account diagram topologies. For instance, it has been recently pointed out [133] that for small orders $n \lesssim 13$ (which are usually sufficient to obtain accurate enough results) an explicit sum over a pre-compiled list of topologies might be more efficient than the determinantal formalism. My implementation has been coded in order to allow an easy replacement of the topology-related routines: this will allow me to keep my code up-to-date with the latest developments in the field.

# Chapter 5

# Conclusions

*In this section the conclusions of this thesis are drawn, summarizing the results and outlining directions for my future work.*

The focus of my thesis is the study of strongly correlated systems of interest for both Condensed Matter and Atomic physics. This task is nontrivial, due to the high complexity of the problems, requiring the use of powerful numerical techniques.

I employ Path Integral Monte Carlo (PIMC) with worm updates, in an implementation written by myself, to study a system of hardcore bosons on a triangular lattice. Here, the interparticle interaction is of interest for experimental realizations with Rydberg-dressed atoms. The adopted numerical technique is a state-of-the-art approach for unfrustrated bosonic systems, allowing accurate measurements of quantities such as, e.g., superfluid densities.

In my work [14] I demonstrate the existence of glass and superglass phases, obtained via temperature quenches in the intermediate- and strong-interaction regime, respectively. These states appear as the out-of-equilibrium counterparts of a crystal and supersolid phase, respectively, and are obtained in the absence of built-in frustration sources in the Hamiltonian, usually employed to obtain glassy behavior. Here, glassy physics arises from the formation of self-assembled particle clus-

ters, which ultimately induce an effective polidispersity in the system.

I also study the model of [14] with longer-range interactions on a square lattice. Preliminary results [54] show a phase transition between a supersolid and a disordered, non-superfluid phase. Large-scale and low-temperature simulations are currently running to understand if, e.g., superfluidity and structural order superfluidity disappear at the same time or if an intermediate phase is present, and to investigate possible temperature and size dependences of the aforementioned physical picture.

The simplicity of the investigated model, as well as its aforementioned relevance for experiments with cold atoms, should pave the way for the experimental realization of the phases predicted in my work.

PIMC techniques cannot be used to reliably study fermionic systems, whose investigation requires other approaches. For instance, Variational Monte Carlo (VMC) can yield high accuracy results for the ground-state properties given a powerful ansatz is chosen as trial wavefunction.

I show [21] that the Entangled Plaquette States (EPS) ansatz can be adapted to investigate the $t-J$ model in the presence of two holes. I demonstrate the existence of a two-hole $d$-wave bound state in the parameter region $0.4 \leq J/t \leq 2.0$, and I find a critical value $J_c/t \lesssim 0.19$ below which a bound state with the same symmetry does not occur.

The main objective of my study on the $t-J$ model has been that of unambiguously demonstrate how the EPS wavefunction can faithfully describe fermionic problems where other approaches suffer from severe limitations, offering also accurate quantitative predictions on various observables of interest.

A further approach to the study of fermionic systems is Diagrammatic Monte Carlo (DMC). This is a finite-temperature numerical technique which has recently elicited considerable interest (see, e.g., [22, 61, 62]) and has seen application to long-standing problems in condensed matter physics, such as, e.g., the investigation of the phase diagram of the 2D Hubbard model [63].

I have coded an implementation of DMC, currently under testing. While currently specialized for the study of the Hubbard model, with

the usual on-site interactions, my algorithm allows the study, on the same footing, of fermionic systems with extended-range interactions.

Problems I am in the position to study in the future include the investigation of ladder systems with the same interaction adopted for the model of section 3.1, to observe how the 2D physics emerges from the one-dimensional scenario [104]. The extension of the EPS ansatz to the case of finite hole concentration in the $t - J$ model is also a possible direction for my future research. In addition, DMC will offer me a further possibility to investigate, e.g., the fermionic counterpart of the extended Bose-Hubbard Hamiltonian studied in section 3.1.

I am very confident that the knowledge about numerical methods that I acquired during my Ph. D. will allow me to carry on my future research by means of very accurate, state-of-the-art tools.

# Résumé

## Introduction

Mon travail de thèse s'axe sur l'étude, par moyen de techniques numériques, de systèmes *fortement corrélés* (c'est-à-dire, dont le comportement ne peut pas être décrit en terme d'entités indépendantes). Ces derniers offrent la possibilité d'observer certains des scénarios les plus intéressants en Physique de la Matière Condensée, qui comprennent en particulier plusieurs exemples de *phénomène quantique macroscopique* (PQM), manifestations a grande échelle des propriétés quantiques du système.

La *superfluidité*, c'est–à–dire la propriété d'un matériel qui soutient un flux de matière persistant et sans dissipation, est un exemple important de PQM, observé en systèmes bosoniques. Rencontrée pour la première fois dans l'Hélium–4 [1, 2], la superfluidité a été ensuite liée à autres types de scénarios physiques, comme la *supersolidité* (p. ex. [3]), la coexistence de superfluidité et ordre structurel dans le matériel. Cette phase exotique avait été proposée pour l'état fondamental de l'Hélium–4 solide, mais cette hypothèse a été démentie par plusieurs études, à la fois numériques [9, 10] et expérimentales [11]. Par contre, supersolides ont été observés, par moyen de techniques numériques, en plusieurs systèmes de bosons, allant de modèles sur réseau (p. ex. [12]) à Hamiltoniens avec interactions à portée étendue en espace libre (p. ex. [13]).

Récemment, l'étude des systèmes fortement corrélés et des scénarios physique leur associés a été relancée grâce à l'idée de *simulation quan-*

*tique* (p. ex. [23, 24]), c'est–à–dire la création d'une expérience qui met en place un Hamiltonien d'intérêt (par exemple, un modèle candidat pour décrire un phénomène inexpliqué) d'une façon contrôlée.

Dans ce domaine, les atomes froids (p. ex. [26, 27]) ont devenu une des plateformes les plus prometteuses, grâce au haute niveau de contrôlabilité atteint en leur manipulation expérimentale: un des systèmes les plus intéressants de ce point de vue sont les atomes froids en états *Rydberg–dressed* (p. ex. [41, 42, 43, 44, 45, 46, 47, 48, 49, 50]), c'est–à–dire en une superposition de l'état fondamental atomique et d'un état excité avec un nombre quantique principal très élevé [connu sous le nom d'*état Rydberg* (p. ex. [38, 39, 40])]. Leur réalisation expérimentale (p. ex. [48, 49]) offre la possibilité d'effectuer simulations quantiques de systèmes avec interactions à portée étendue, qui ont déjà été liés à phénomènes physiques exotiques par études théoriques (p. ex. [13]).

La recherche de phases exotiques (supersolides, et en générale phases qui montrent coexistence de plusieurs paramètres d'ordre) dans systèmes pertinents pour expériences avec atomes en états Rydberg–dressed est une des directions de mon travail de thèse. J'expose les résultats que j'ai obtenu en suivant cette ligne de recherche [14] en Section 1.

Un autre exemple de PQM, observé en systèmes de fermions, est la *supraconductivité*: plusieurs matériaux, au–dessous d'une température $T_c$, subissent une transition de phase, manifestant une résistance électrique nulle et des propriétés magnétiques particulières. Certaines entre ces matériaux (appelés *conventionnels*) sont bien décrits par la *théorie Bardeen–Cooper–Schrieffer (BCS)* [15] : par contre, une théorie pour expliquer le comportement supraconducteur dans les autres (connus sous le nom de *supraconducteurs à haute température*) n'a pas encore été établie (p. ex. [16, 17, 18]).

Hamiltoniens fermioniques fortement corrélés comme le modèle d'Hubbard ou le $t - J$ ont été proposés comme candidats [19] pour décrire ces matériaux : cependant, la relation entre les modèles et le phénomène physique n'est encore entièrement claire. Une des raisons pour cette situation est le fait que la grande partie des techniques numériques utilisées pour étudier les systèmes fortement corrélés ne peuvent pas

être appliquées dans le cas de ces Hamiltoniens : par exemple, les techniques de Path Integral Monte Carlo (PIMC), très puissants en l'étude de systèmes de bosons, souffrent des lourdes instabilités numériques, connues sous le nom de *sign problem* [20].

L'étude d'Hamiltoniens fortement corrélés de fermions, et le développement de nouveaux méthodes numériques dans ce but, est une autre direction de mon travail de thèse : les résultats que j'ai obtenu en suivant cette ligne de recherche [21] sont exposés en Section 2.

## 1. Systèmes Bosoniques

L'étude des systèmes désordonnés est très intéressante pour la Physique de la Matière Condensée: généralement, le désordre est introduit en utilisant des sources de frustration ajoutées *ad-hoc* au système, qui génèrent des phénomènes de localisation et des phases isolantes ([73], [85]). Par la suite, on appellera *verre* un état de la matière manifestant de la localisation en l'absence d'ordre structurel (contrairement à un cristal, qui a une structure ordonnée).

Bien que la majorité des phénomènes causés par le désordre possèdent un caractère isolant, des études numériques ont montré la possibilité d'une coexistence entre phases vitreuses et effets quantiques (Condensation de Bose–Einstein ou Superfluidité), comme dans le cas des Supersolides. Ces nouvelles phases de la matière sont nommées *superverres*, et ont été observées numériquement avec de l'Hélium–4 subissant une procédure de quench [88] et dans systèmes sur réseaux frustrés [53].

Malgré ces résultats numériques, la phase supervitreuse n'a pas encore été observée expérimentalement, aussi en raison de la grande valeur de frustration devant être implémentée dans l'Hamiltonien pour systèmes sur réseau (comme dans [53]). Par conséquent, la possibilité d'observer des superverres avec un Hamiltonien invariant par translation (sans sources de frustration ajoutées) ainsi que leur praticabilité expérimentale, restent encore des questions ouvertes.

J'ai répondu à ces questions [14] en étudiant un système de bosons cœur–dur interagissants sur un réseau triangulaire. L'Hamiltonien considéré est invariant par translations (aucune source de frustration a été ajoutée) et les bosons interagissent au moyen d'une interaction densité–densité à portée étendue reproduisant les caractéristiques principales de l'interaction entre atomes en états Rydberg–dressed [41].

J'ai étudié mon système via des simulations PIMC avec les Worm Updates [52]. Cette méthode est numériquement exacte pour n'importe quel système de bosons non frustrés. L'implémentation utilisée dans mon travail a été effectuée par mes soins. Pour caractériser les phases que j'ai rencontré j'ai utilisé les paramètres d'ordre suivants:

- La *Fraction Superfluide* $\rho_s$, non nulle en systèmes superfluides.
- Le *Facteur de Structure* $S(\boldsymbol{k})$, possédant des pics non triviaux en présence d'ordre structurel dans le système.
- Le *Paramètre d'Edwards–Anderson* $\widetilde{q}_{\mathrm{EA}}$ [53], dont une valeur non nulle en l'absence d'ordre structurel identifie le comportement vitreux.

J'ai obtenu un diagramme de phase à l'équilibre comprenant une phase liquide à haute température et une phase *superfluide*, un *supersolide* et un *cristal* pour interactions faibles, moyennes et forts respectivement, à basse température.

Le superfluide se distingue du liquide par une valeur de $\rho_s$ non nulle, tandis que $S(\boldsymbol{k})$ et $\widetilde{q}_{\mathrm{EA}}$ sont nuls dans les deux cas. Une valeur intermédiaire des interactions provoque l'apparition d'ordre structurel (et donc un $S(\boldsymbol{k})$ non nul) en coexistence avec la superfluidité. Pour interactions fortes, la fraction superfluide disparait tandis que $S(\boldsymbol{k})$ reste non nul, entrainant une phase cristalline.

Par la suite, j'ai exploré la physique hors d'équilibre du système. Dans ce but, j'ai effectué des simulations de *quench* (soudain refroidissements du système, effectués trop vite pour permettre au système de s'équilibrer). Pour des quench suffisamment forts, le système ne peut plus s'équilibrer, et reste "bloqué" dans des états métastables. Cette

métastabilité est démontré par le fait que différentes réalisations de la même simulation (avec différentes conditions initiales et suites aléatoires de thermalisation) conduisent à différents états métastables.

J'ai effectué des simulations de quench dans les régions supersolide et solide du diagramme de phase d'équilibre. Dans les deux cas, la valeur moyenne sur les réalisations de $\max_{\boldsymbol{k}} S(\boldsymbol{k})$ diminue rapidement avec la taille du système, à cause du nombre croissant de réalisations qui restent bloquées dans des états métastables désordonnés. En même temps, $\widetilde{q}_{\mathrm{EA}}$ (dans les deux cas) et $\rho_s$ (dans la région supersolide à l'équilibre) restent non nuls.

Ces résultats amènent à la conclusion que, en présence d'un quench, le système est amené hors d'équilibre, et arrive dans des états localisés mais désordonnés, isolants ($\rho_s = 0$) pour interactions fortes, et superfluides ($\rho_s \neq 0$) pour des interactions intermédiaires. Ces états correspondent à la définition donnée auparavant de verre et superverre.

La cause de l'apparition de ces états est la formation spontanée (à densité suffisamment haute) de *clusters*. Ces derniers sont groupes de particules qui prennent le rôle de degrés de liberté efficaces du système. Ils varient en forme, orientation et nombre de composants : cette variété génère une polydispersité efficace qui se comporte comme une source de frustration, en causant l'apparition de (super)verres en l'absence de sources de frustration externes ajoutées au système.

En conclusion, dans la partie de mon travail consacré à l'étude de systèmes de bosons j'ai examiné un système avec interactions reproduisant les caractéristiques principales de l'interaction entre atomes de Rydberg. Mon résultat principal est la démonstration de l'existence de régions où la physique vitreuse et la superfluidité coexistent. Ces régions de superverre sont obtenues hors d'équilibre, en l'absence de sources de frustration ajoutées au système et avec un Hamiltonien expérimentalement pertinent.

J'ai aussi étudié [54] le même modèle sur un réseau carré et avec une portée d'interaction augmentée, jusqu'à tailles de $48 \times 48$ sites et températures de $T/t = 1/20$ (où $t$ est le paramètre de saut dans l'Hamiltonien). Résultats préliminaires ont montré une transition de phase entre un su-

persolide et un état non–superfluide et désordonné avec une fonction de Green qui montre un comportement à loi de puissance à grande distance. Simulations à grandes tailles et basses températures sont en cours pour comprendre si, par exemple, l'ordre structurel et la superfluidité disparaissent en même temps ou une phase intermédiaire est présente, et pour étudier la dépendance en taille et température des phénomènes susmentionnés.

## 2. Systèmes Fermioniques

J'ai étudié [21] le modèle $t - J$ sûr le réseau carré en présence de deux trous par rapport à l'état de demi–remplissage (une particule par site). Étudier numériquement le modèle $t - J$ est difficile à cause de sa nature fermionique et fortement corrélée: j'ai utilisé la célèbre méthode de *Monte Carlo Variationnel* avec l'ansatz EPS (*Entangled Plaquette States*) [69]. Mes objectifs principaux ont étés la démonstration de la possibilité d'application de l'ansatz EPS pour étudier Hamiltoniens de fermions fortement corrélés, où beaucoup d'autres techniques numériques sont inapplicables, ainsi que la compréhension du comportement physique de l'état fondamental du système.

Dans mon travail, j'ai étudié le modèle $t - J$ dans la fourchette de paramètres $0.4 \leq J/t \leq 2.0$ (dans l'Hamiltonien, $J$ est le coefficient du terme d'interaction et $t$ est le paramètre de saut). Mes résultats sont en très bon accord avec la diagonalisation exacte [123] à petite taille. À tailles modérées, je trouve bon accord avec les résultats de la méthode de Green Function Monte Carlo (GFMC) [55] : cette technique peut être appliqué seulement à prix d'approximations qui limitent la taille maximale d'application et la précision des résultats. Par contre, la méthode EPS ne souffre pas de ces problèmes, en produisant à tailles relativement grandes des résultats variationnels qui peuvent être compté parmi les plus précis et fiables pour le modèle $t - J$.

J'ai démontré, en calculant l'énergie de liaison des trous et la fonction de distribution de leur distance relative, l'existence d'un état lié de trous avec symétrie $d_{x^2-y^2}$ pour tous les valeurs de $J/t$ que j'ai considéré.

En utilisant l'énergie de liaison des trous, j'ai estimé qu'un état lié avec cette symétrie disparaît pour $J/t < J_c/t \simeq 0.19$.

Étant donné la précision des résultats obtenus par moyen de l'ansatz EPS, mon travail est séminal pour l'application de cette technique à l'étude d'autres systèmes de fermions fortement corrélés, où autres méthodes comme le GFMC ne peuvent pas être appliqués, comme par exemple le modèle $t - J$ dans le cas de concentration de trous finie (où différentes études numériques, p. ex. [59, 60]) sont en contradiction en ce qui concerne la nature de l'état fondamental du système).

Dans mon travail de thèse j'ai aussi programmé une implémentation de l'algorithme de Monte Carlo Diagrammatique (p. ex. [22]), selon l'approche proposée en [62]. Cette technique est une des méthodes les plus prometteuses pour l'étude de systèmes fermioniques fortement corrélés (p. ex., [63]). Mon code est à présent en phase d'essai ; une fois complété, il m'offrira la possibilité de traiter interactions à portée à la fois courte et étendue. Cette capacité me permettra d'étudier plusieurs modèles fermioniques d'intérêt (par exemple, l'homologue fermionique du modèle considéré en Section 1, pour comprendre de quelle façon le diagramme de phase du système est influencé par la statistique des particules).

# Bibliography


[1] P. Kapitza, "Viscosity of liquid helium below the $\lambda$-point," *Nature*, vol. 141, no. 3558, pp. 74–74, 1938.

[2] J. F. Allen and M. A. D., "Flow phenomena in liquid helium ii," *Nature*, vol. 142, no. 3597, pp. 643–644, 1938.

[3] M. Boninsegni and N. V. Prokof'ev, "Colloquium: Supersolids: What and where are they?" *Rev. Mod. Phys.*, vol. 84, pp. 759–776, 2012.

[4] K. W. Madison, F. Chevy, W. Wohlleben, and J. Dalibard, "Vortex formation in a stirred bose-einstein condensate," *Phys. Rev. Lett.*, vol. 84, pp. 806–809, 2000.

[5] A. F. Andreev and I. M. Lifshitz, "Quantum theory of defects in crystals," *Journal of Experimental and Theoretical Physics*, vol. 29, pp. 1107–1113, 1969.

[6] G. V. Chester, "Speculations on bose-einstein condensation and quantum crystals," *Phys. Rev. A*, vol. 2, pp. 256–258, 1970.

[7] E. Kim and M. H. W. Chan, "Probable observation of a supersolid helium phase," *Nature*, vol. 427, no. 6971, pp. 225–227, 2004.

[8] E. Kim, "Observation of superflow in solid helium," *Science*, vol. 305, no. 5692, pp. 1941–1944, 2004.

[9] D. M. Ceperley and B. Bernu, "Ring exchanges and the supersolid phase of $^4$He," *Phys. Rev. Lett.*, vol. 93, p. 155 303, 2004.

[10] M. Boninsegni, A. B. Kuklov, L. Pollet, N. V. Prokof'ev, B. V. Svistunov, and M. Troyer, "Fate of vacancy-induced supersolidity in $^4$He," *Phys. Rev. Lett.*, vol. 97, p. 080 401, 2006.

[11] D. Y. Kim and M. H. W. Chan, "Absence of supersolidity in solid helium in porous vycor glass," *Phys. Rev. Lett.*, vol. 109, p. 155 301, 2012.

[12] M. Boninsegni and N. Prokof'ev, "Supersolid phase of hard-core bosons on a triangular lattice," *Phys. Rev. Lett.*, vol. 95, p. 237 204, 2005.

[13] F. Cinti, T. Macrí, W. Lechner, G. Pupillo, and T. Pohl, "Defect-induced supersolidity with soft-core bosons," *Nature communications*, vol. 5, no. 3235, 2014.

[14] A. Angelone, F. Mezzacapo, and G. Pupillo, "Superglass phase of interaction-blockaded gases on a triangular lattice," *Phys. Rev. Lett.*, vol. 116, p. 135 303, 2016.

[15] J. Bardeen, L. N. Cooper, and J. R. Schrieffer, "Theory of superconductivity," *Phys. Rev.*, vol. 108, pp. 1175–1204, 1957.

[16] E. Dagotto, "Correlated electrons in high-temperature superconductors," *Rev. Mod. Phys.*, vol. 66, pp. 763–840, 1994.

[17] P. A. Lee, N. Nagaosa, and X.-G. Wen, "Doping a mott insulator: Physics of high-temperature superconductivity," *Rev. Mod. Phys.*, vol. 78, pp. 17–85, 2006.

[18] B. Keimer, S. A. Kivelson, M. R. Norman, S. Uchida, and J. Zaanen, "From quantum matter to high-temperature superconductivity in copper oxides," *Nature*, vol. 518, no. 7538, pp. 179–186, 2015.

[19] P. W. Anderson, "The resonating valence bond state in la2cuo4 and superconductivity," *Science*, vol. 235, no. 4793, pp. 1196–1198, 1987.

[20] M. Troyer and U.-J. Wiese, "Computational complexity and fundamental limitations to fermionic quantum monte carlo simulations," *Phys. Rev. Lett.*, vol. 94, p. 170 201, 2005.

[21] F. Mezzacapo, A. Angelone, and G. Pupillo, "Two holes in a two-dimensional quantum antiferromagnet: A variational study based on entangled-plaquette states," *Phys. Rev. B*, vol. 94, p. 155 120, 2016.

[22] K. Van Houcke, E. Kozik, N. Prokof'ev, and B. Svistunov, "Diagrammatic monte carlo," *Physics Procedia*, vol. 6, pp. 95–105, 2010.

[23] I. M. Georgescu, S. Ashhab, and F. Nori, "Quantum simulation," *Rev. Mod. Phys.*, vol. 86, pp. 153–185, 2014.

[24] J. I. Cirac and P. Zoller, "Goals and opportunities in quantum simulation," *Nature Physics*, vol. 8, no. 4, pp. 264–266, 2012.

[25] R. P. Feynman, "Simulating physics with computers," *International Journal of Theoretical Physics*, vol. 21, pp. 467–488, 1982.

[26] I. Bloch, J. Dalibard, and W. Zwerger, "Many-body physics with ultracold gases," *Rev. Mod. Phys.*, vol. 80, pp. 885–964, 2008.

[27] I. Bloch, J. Dalibard, and S. Nascimbene, "Quantum simulations with ultracold quantum gases," *Nature Physics*, vol. 8, no. 4, pp. 267–276, 2012.

[28] M. H. Anderson, J. R. Ensher, M. R. Matthews, C. E. Wieman, and E. A. Cornell, "Observation of bose-einstein condensation in a dilute atomic vapor," *science*, vol. 269, no. 5221, p. 198, 1995.

[29] K. B. Davis, M. O. Mewes, M. R. Andrews, N. J. van Druten, D. S. Durfee, D. M. Kurn, and W. Ketterle, "Bose-einstein condensation in a gas of sodium atoms," *Phys. Rev. Lett.*, vol. 75, pp. 3969–3973, 1995.

[30] C. C. Bradley, C. A. Sackett, J. J. Tollett, and R. G. Hulet, "Evidence of bose-einstein condensation in an atomic gas with attractive interactions," *Phys. Rev. Lett.*, vol. 75, pp. 1687–1690, 1995.

[31] M. W. Zwierlein, J. R. Abo-Shaeer, A. Schirotzek, C. H. Schunck, and W. Ketterle, "Vortices and superfluidity in a strongly interacting fermi gas," *Nature*, vol. 435, no. 7045, pp. 1047–1051, 2005.

[32] S. Trotzky, L. Pollet, F. Gerbier, U. Schnorrberger, I. Bloch, N. V. Prokof'ev, B. Svistunov, and M. Troyer, "Suppression of the critical temperature for superfluidity near the mott transition," *Nature Physics*, vol. 6, no. 12, pp. 998–1004, 2010.

[33] C. Chin, R. Grimm, P. Julienne, and E. Tiesinga, "Feshbach resonances in ultracold gases," *Rev. Mod. Phys.*, vol. 82, pp. 1225–1286, 2010.

[34] M. Randeria and E. Taylor, "Crossover from bardeen-cooper-schrieffer to bose-einstein condensation and the unitary fermi gas," *Annual Review of Condensed Matter Physics*, vol. 5, pp. 209–232, 2014.

[35] C. A. Regal, M. Greiner, and D. S. Jin, "Observation of resonance condensation of fermionic atom pairs," *Phys. Rev. Lett.*, vol. 92, p. 040 403, 2004.

[36] T. Lahaye, C. Menotti, L. Santos, M. Lewenstein, and T. Pfau, "The physics of dipolar bosonic quantum gases," *Reports on Progress in Physics*, vol. 72, no. 12, p. 126 401, 2009.

[37] J. Doyle, B. Friedrich, R. V. Krems, and F. Masnou-Seeuws, "Editorial: Quo vadis, cold molecules?" *The European Physical Journal D - Atomic, Molecular, Optical and Plasma Physics*, vol. 31, no. 2, pp. 149–164, 2004.

[38] T. F. Gallagher, *Rydberg Atoms*, ser. Cambridge Monographs on Atomic, Molecular and Chemical Physics. Cambridge University Press, 1994.

[39] R. Löw, H. Weimer, J. Nipper, J. B. Balewski, B. Butscher, H. P. Büchler, and T. Pfau, "An experimental and theoretical guide to strongly interacting rydberg gases," *Journal of Physics B: Atomic, Molecular and Optical Physics*, vol. 45, no. 11, p. 113 001, 2012.

[40] J. Lim, H.-G. Lee, and J. Ahn, "Review of cold rydberg atoms and their applications," *Journal of the Korean Physical Society*, vol. 63, no. 4, pp. 867–876, 2013.

[41] N. Henkel, R. Nath, and T. Pohl, "Three-dimensional roton excitations and supersolid formation in rydberg-excited bose-einstein condensates," *Phys. Rev. Lett.*, vol. 104, p. 195 302, 2010.

[42] F. Cinti, P. Jain, M. Boninsegni, A. Micheli, P. Zoller, and G. Pupillo, "Supersolid droplet crystal in a dipole-blockaded gas," *Phys. Rev. Lett.*, vol. 105, p. 135 301, 2010.

[43] L. Santos, G. V. Shlyapnikov, P. Zoller, and M. Lewenstein, "Bose-einstein condensation in trapped dipolar gases," *Phys. Rev. Lett.*, vol. 85, pp. 1791–1794, 2000.

[44] J. Honer, H. Weimer, T. Pfau, and H. P. Büchler, "Collective many-body interaction in rydberg dressed atoms," *Phys. Rev. Lett.*, vol. 105, p. 160 404, 2010.

[45] G. Pupillo, A. Micheli, M. Boninsegni, I. Lesanovsky, and P. Zoller, "Strongly correlated gases of rydberg-dressed atoms: Quantum and classical dynamics," *Phys. Rev. Lett.*, vol. 104, p. 223 002, 2010.

[46] N. Henkel, F. Cinti, P. Jain, G. Pupillo, and T. Pohl, "Supersolid vortex crystals in rydberg-dressed bose-einstein condensates," *Phys. Rev. Lett.*, vol. 108, p. 265 301, 2012.

[47] T. Macrí and T. Pohl, "Rydberg dressing of atoms in optical lattices," *Phys. Rev. A*, vol. 89, p. 011 402, 2014.

[48] Y.-Y. Jau, A. M. Hankin, T. Keating, I. H. Deutsch, and G. W. Biedermann, "Entangling atomic spins with a rydberg-dressed spin-flip blockade," *Nature Physics*, vol. 12, no. 1, pp. 71–74, 2015.

[49] J. Zeiher, R. van Bijnen, P. Schauß, S. Hild, J.-Y. Choi, T. Pohl, I. Bloch, and C. Gross, "Many-body interferometry of a rydberg-dressed spin-lattice," *Nature Physics*, vol. 12, no. 12, pp. 1095–1099, 2016.

[50] S. Helmrich, A. Arias, N. Pehoviak, and S. Whitlock, "Two-body interactions and decay of three-level rydberg-dressed atoms," *Journal of Physics B: Atomic, Molecular and Optical Physics*, vol. 49, no. 3, 2016.

[51] J. E. Johnson and S. L. Rolston, "Interactions between rydberg-dressed atoms," *Phys. Rev. A*, vol. 82, p. 033 412, 2010.

[52] N. V. Prokof'ev, B. V. Svistunov, and I. S. Tupitsyn, "Exact, complete, and universal continuous-time worldline monte carlo approach to the statistics of discrete quantum systems," *Journal of Experimental and Theoretical Physics*, vol. 87, no. 2, pp. 310–321, 1998.

[53] G. Carleo, M. Tarzia, and F. Zamponi, "Bose-einstein condensation in quantum glasses," *Phys. Rev. Lett.*, vol. 103, p. 215 302, 2009.

[54] T. Ying, M. Dalmonte, A. Angelone, F. Mezzacapo, P. Zoller, and G. Pupillo, *Cluster bose metals*, 2016. eprint: arXiv:1606.04267.

[55] M. Boninsegni and E. Manousakis, "Two-hole d-wave binding in the physical region of the t-j model: A green's-function monte carlo study," *Phys. Rev. B*, vol. 47, pp. 11 897–11 904, 1993.

[56] J.-I. Inoue and S. Maekawa, "Dynamics of two holes in the t-j model," *Progress of Theoretical Physics Supplement*, vol. 108, pp. 313–326, 1992.

[57] L. Vidmar and J. Bonča, "Two holes in the t–j model form a bound state for any nonzero $J/t$," *Journal of Superconductivity and Novel Magnetism*, vol. 26, no. 8, pp. 2641–2645, 2013.

[58] P. Corboz, S. R. White, G. Vidal, and M. Troyer, "Stripes in the two-dimensional $t$-$J$ model with infinite projected entangled-pair states," *Phys. Rev. B*, vol. 84, p. 041 108, 2011.

[59] W.-J. Hu, F. Becca, and S. Sorella, "Absence of static stripes in the two-dimensional $t - J$ model determined using an accurate and systematic quantum monte carlo approach," *Phys. Rev. B*, vol. 85, p. 081 110, 2012.

[60] P. Corboz, T. M. Rice, and M. Troyer, "Competing states in the $t$-$J$ model: Uniform $d$-wave state versus stripe state," *Phys. Rev. Lett.*, vol. 113, p. 046 402, 2014.

[61] S. A. Kulagin, N. Prokof'ev, O. A. Starykh, B. Svistunov, and C. N. Varney, "Bold diagrammatic monte carlo technique for frustrated spin systems," *Phys. Rev. B*, vol. 87, p. 024 407, 2013.

[62] R. Rossi, *Determinant diagrammatic monte carlo in the thermodynamic limit*, 2016. eprint: arXiv:1612.05184.

[63] Y. Deng, E. Kozik, N. V. Prokof'ev, and B. V. Svistunov, "Emergent bcs regime of the two-dimensional fermionic hubbard model: Ground-state phase diagram," *EPL (Europhysics Letters)*, vol. 110, no. 5, p. 57 001, 2015.

[64] A. W. Sandvik, "An introduction to quantum monte carlo methods," in *Strongly Correlated Magnetic and Superconducting Systems: Proceedings of the El Escorial Summer School Held in Madrid, Spain, 15–19 July 1996*, G. Sierra and M. A. Martín-Delgado, Eds. Berlin, Heidelberg: Springer Berlin Heidelberg, 1997, pp. 109–135, ISBN: 978-3-540-49734-9.

[65] N. Metropolis, A. W. Rosenbluth, M. N. Rosenbluth, A. H. Teller, and E. Teller, "Equation of state calculations by fast computing machines," *The Journal of Chemical Physics*, vol. 21, pp. 1087–, 1953.

[66] L. Pollet, "Recent developments in quantum monte carlo simulations with applications for cold gases," *Reports on Progress in Physics*, vol. 75, no. 9, p. 094 501, 2012.

[67] V. G. Rousseau, "Superfluid density in continuous and discrete spaces: Avoiding misconceptions," *Phys. Rev. B*, vol. 90, p. 134 503, 13 2014.

[68] J. Toulouse, R. Assaraf, and C. J. Umrigar, *Introduction to the variational and diffusion monte carlo methods*, 2015. eprint: arXiv:1508.02989.

[69] F. Mezzacapo, N. Schuch, M. Boninsegni, and J. I. Cirac, "Ground-state properties of quantum many-body systems: Entangled-plaquette states and variational monte carlo," *New Journal of Physics*, vol. 11, no. 8, p. 083 026, 2009.

[70] F. Mezzacapo and J. I. Cirac, "Ground–state properties of the spin–$\frac{1}{2}$ antiferromagnetic heisenberg model on the triangular lattice: A variational study based on entangled-plaquette states," *New Journal of Physics*, vol. 12, no. 10, p. 103 039, 2010.

[71] F. Mezzacapo and M. Boninsegni, "Ground-state phase diagram of the quantum $J_1 - J_2$ model on the honeycomb lattice," *Phys. Rev. B*, vol. 85, p. 060 402, 2012.

[72] F. Mezzacapo, "Variational study of a mobile hole in a two-dimensional quantum antiferromagnet using entangled-plaquette states," *Phys. Rev. B*, vol. 83, p. 115 111, 2011.

[73] P. W. Anderson, "Absence of diffusion in certain random lattices," *Phys. Rev.*, vol. 109, pp. 1492–1505, 1958.

[74] A. Lagendijk, B. van Tiggelen, and D. S. Wiersma, "Fifty years of anderson localization," *Physics Today*, vol. 62, no. 8, pp. 24–29, 2009.

[75] E. Hamza, R. Sims, and G. Stolz, "Dynamical localization in disordered quantum spin systems," *Communications in Mathematical Physics*, vol. 315, no. 1, pp. 215–239, 2012.

[76] D. M. Basko, I. L. Aleiner, and B. L. Altshuler, "Metal–insulator transition in a weakly interacting many-electron system with localized single-particle states," *Annals of Physics*, vol. 321, pp. 1126–1205, 2006.

[77] R. Nandkishore and D. A. Huse, "Many-body localization and thermalization in quantum statistical mechanics," *Annual Review of Condensed Matter Physics*, vol. 6, no. 1, pp. 15–38, 2015.

[78] B. Damski, J. Zakrzewski, L. Santos, P. Zoller, and M. Lewenstein, "Atomic bose and anderson glasses in optical lattices," *Phys. Rev. Lett.*, vol. 91, p. 080 403, 2003.

[79] J. Billy, V. Josse, Z. Zuo, A. Bernard, B. Hambrecht, P. Lugan, D. Clément, L. Sanchez-Palencia, P. Bouyer, and A. Aspect, "Direct observation of anderson localization of matter waves in a controlled disorder," *Nature*, vol. 453, pp. 891–894, 2008.

[80] L. Sanchez-Palencia, D. Clément, P. Lugan, P. Bouyer, and A. Aspect, "Disorder-induced trapping versus anderson localization in bose–einstein condensates expanding in disordered potentials," *New Journal of Physics*, vol. 10, no. 4, p. 045 019, 2008.

[81] G. Roati, C. D'Errico, L. Fallani, M. Fattori, C. Fort, M. Zaccanti, G. Modugno, M. Modugno, and M. Inguscio, "Anderson localization of a non-interacting bose–einstein condensate," *Nature*, vol. 453, no. 7197, pp. 895–898, 2008.

[82] M. White, M. Pasienski, D. McKay, S. Q. Zhou, D. Ceperley, and B. DeMarco, "Strongly interacting bosons in a disordered optical lattice," *Phys. Rev. Lett.*, vol. 102, p. 055 301, 2009.

[83] A. M. Goldman and N. Marković, "Superconductor-insulator transitions in the two-dimensional limit," *Physics Today*, vol. 51, no. 11, pp. 39–44, 1998.

[84] A. S. C. Rittner and J. D. Reppy, "Disorder and the supersolid state of solid $^4$He," *Phys. Rev. Lett.*, vol. 98, p. 175 302, 2007.

[85] M. P. A. Fisher, P. B. Weichman, G. Grinstein, and D. S. Fisher, "Boson localization and the superfluid-insulator transition," *Phys. Rev. B*, vol. 40, pp. 546–570, 1989.

[86] W. Krauth, N. Trivedi, and D. Ceperley, "Superfluid-insulator transition in disordered boson systems," *Phys. Rev. Lett.*, vol. 67, pp. 2307–2310, 1991.

[87] L. Pollet, N. V. Prokof'ev, B. V. Svistunov, and M. Troyer, "Absence of a direct superfluid to mott insulator transition in disordered bose systems," *Phys. Rev. Lett.*, vol. 103, p. 140 402, 2009.

[88] M. Boninsegni, N. Prokof'ev, and B. Svistunov, "Superglass phase of $^4$He," *Phys. Rev. Lett.*, vol. 96, p. 105 301, 2006.

[89] B. Hunt, E. Pratt, V. Gadagkar, M. Yamashita, A. V. Balatsky, and J. C. Davis, "Evidence for a superglass state in solid 4he," *Science*, vol. 324, no. 5927, pp. 632–636, 2009.

[90] J. T. West, O. Syshchenko, J. Beamish, and M. H. W. Chan, "Role of shear modulus and statistics in the supersolidity of helium," *Nature Physics*, vol. 5, no. 8, pp. 598–601, 2009.

[91] G. Biroli, C. Chamon, and F. Zamponi, "Theory of the superglass phase," *Phys. Rev. B*, vol. 78, p. 224 306, 2008.

[92] L. Dang, M. Boninsegni, and L. Pollet, "Disorder-induced superfluidity," *Phys. Rev. B*, vol. 79, p. 214 529, 2009.

[93] D. Larson and Y.-J. Kao, "Tuning the disorder in superglasses," *Phys. Rev. Lett.*, vol. 109, p. 157 202, 2012.

[94] G. Murthy, D. Arovas, and A. Auerbach, "Superfluids and supersolids on frustrated two-dimensional lattices," *Phys. Rev. B*, vol. 55, pp. 3104–3121, 1997.

[95] M. Boninsegni, "Hard core bosons on a triangular lattice," *Journal of Low Temperature Physics*, vol. 132, no. 1, pp. 39–53, 2003.

[96] R. G. Melko, A. Paramekanti, A. A. Burkov, A. Vishwanath, D. N. Sheng, and L. Balents, "Supersolid order from disorder: Hard-core bosons on the triangular lattice," *Phys. Rev. Lett.*, vol. 95, p. 127 207, 2005.

[97] S. Wessel and M. Troyer, "Supersolid hard-core bosons on the triangular lattice," *Phys. Rev. Lett.*, vol. 95, p. 127 205, 2005.

[98] L. Pollet, J. D. Picon, H. P. Büchler, and M. Troyer, "Supersolid phase with cold polar molecules on a triangular lattice," *Phys. Rev. Lett.*, vol. 104, p. 125 302, 2010.

[99] B. Capogrosso-Sansone, C. Trefzger, M. Lewenstein, P. Zoller, and G. Pupillo, "Quantum phases of cold polar molecules in 2d optical lattices," *Phys. Rev. Lett.*, vol. 104, p. 125 301, 2010.

[100] W. Lechner, F. Cinti, and G. Pupillo, "Tunable defect interactions and supersolidity in dipolar quantum gases on a lattice potential," *Phys. Rev. A*, vol. 92, p. 053 625, 2015.

[101] D. A. Lenz, R. Blaak, C. N. Likos, and B. M. Mladek, "Microscopically resolved simulations prove the existence of soft cluster crystals," *Phys. Rev. Lett.*, vol. 109, p. 228 301, 2012.

[102] F. Sciortino and E. Zaccarelli, "Computational materials science: Soft heaps and clumpy crystals," *Nature*, vol. 493, pp. 30–31, 2013.

[103] B. M. Mladek, D. Gottwald, G. Kahl, M. Neumann, and C. N. Likos, "Formation of polymorphic cluster phases for a class of models of purely repulsive soft spheres," *Phys. Rev. Lett.*, vol. 96, p. 045 701, 2006.

[104] M. Mattioli, M. Dalmonte, W. Lechner, and G. Pupillo, "Cluster luttinger liquids of rydberg-dressed atoms in optical lattices," *Phys. Rev. Lett.*, vol. 111, p. 165 302, 2013.

[105] M. Dalmonte, W. Lechner, Z. Cai, M. Mattioli, A. M. Läuchli, and G. Pupillo, "Cluster luttinger liquids and emergent supersymmetric conformal critical points in the one-dimensional soft-shoulder hubbard model," *Phys. Rev. B*, vol. 92, p. 045 106, 2015.

[106] K. Binder and A. P. Young, "Spin glasses: Experimental facts, theoretical concepts, and open questions," *Rev. Mod. Phys.*, vol. 58, pp. 801–976, 1986.

[107] V. G. Rousseau, "Stochastic green function algorithm," *Phys. Rev. E*, vol. 77, p. 056 705, 2008.

[108] M. V. Feigelman, V. B. Geshkenbein, L. B. Ioffe, and A. I. Larkin, "Two-dimensional bose liquid with strong gauge-field interaction," *Phys. Rev. B*, vol. 48, pp. 16 641–16 661, 1993.

[109] P. Phillips and D. Dalidovich, "The elusive bose metal," *Science*, vol. 302, pp. 243–247, 5643 Oct. 2003.

[110] A. W. Tsen, B. Hunt, Y. D. Kim, Z. J. Yuan, S. Jia, R. J. Cava, J. Hone, P. Kim, C. R. Dean, and A. N. Pasupathy, "Nature of the quantum metal in a two-dimensional crystalline superconductor," *Nature Physics*, vol. 12, pp. 208–212, 2016.

[111] O. I. Motrunich and M. P. A. Fisher, "$d$-wave correlated critical bose liquids in two dimensions," *Phys. Rev. B*, vol. 75, p. 235 116, 2007.

[112] W. von der Linden, "A quantum monte carlo approach to many-body physics," *Physics Reports*, vol. 220, no. 2, pp. 53–162, 1992.

[113] R. Orús, "A practical introduction to tensor networks: Matrix product states and projected entangled pair states," *Annals of Physics*, vol. 349, pp. 117–158, 2014.

[114] M. Fannes, B. Nachtergaele, and R. F. Werner, "Finitely correlated states on quantum spin chains," *Comm. Math. Phys.*, vol. 144, no. 3, pp. 443–490, 1992.

[115] S. Östlund and S. Rommer, "Thermodynamic limit of density matrix renormalization," *Phys. Rev. Lett.*, vol. 75, pp. 3537–3540, 1995.

[116] J. Dukelsky, M. A. Martín-Delgado, T. Nishino, and G. Sierra, "Equivalence of the variational matrix product method and the density matrix renormalization group applied to spin chains," *EPL (Europhysics Letters)*, vol. 43, no. 4, p. 457, 1998.

[117] F. Verstraete, D. Porras, and J. I. Cirac, "Density matrix renormalization group and periodic boundary conditions: A quantum information perspective," *Phys. Rev. Lett.*, vol. 93, p. 227 205, 2004.

[118] S. R. White, "Density matrix formulation for quantum renormalization groups," *Phys. Rev. Lett.*, vol. 69, pp. 2863–2866, 1992.

[119] A. W. Sandvik, "Finite-size scaling of the ground-state parameters of the two-dimensional heisenberg model," *Phys. Rev. B*, vol. 56, pp. 11 678–11 690, 1997.

[120] M. Brunner, F. F. Assaad, and A. Muramatsu, "Single-hole dynamics in the $t - J$ model on a square lattice," *Phys. Rev. B*, vol. 62, pp. 15 480–15 492, 2000.

[121] Z. Zhu, H.-C. Jiang, D. N. Sheng, and Z.-Y. Weng, "Nature of strong hole pairing in doped mott antiferromagnets," *Scientific Reports*, vol. 4, no. 1, 2014.

[122] H. J. Changlani, J. M. Kinder, C. J. Umrigar, and G. K.-L. Chan, "Approximating strongly correlated wave functions with correlator product states," *Phys. Rev. B*, vol. 80, p. 245 116, 2009.

[123] T. Barnes, A. E. Jacobs, M. D. Kovarik, and W. G. Macready, "Detailed lanczos study of one- and two-hole band structure and finite-size effects in the t-j model," *Phys. Rev. B*, vol. 45, pp. 256–265, 1992.

[124] E. Dagotto, A. Moreo, F. Ortolani, D. Poilblanc, and J. Riera, "Static and dynamical properties of doped hubbard clusters," *Phys. Rev. B*, vol. 45, pp. 10 741–10 760, 1992.

[125] D. Poilblanc, "Binding of holes and the pair spectral function in the t-j model," *Phys. Rev. B*, vol. 48, pp. 3368–3374, 1993.

[126] L. Vidmar, J. Bonča, S. Maekawa, and T. Tohyama, "Bipolaron in the $t-J$ model coupled to longitudinal and transverse quantum lattice vibrations," *Phys. Rev. Lett.*, vol. 103, p. 186 401, 2009.

[127] E. Kozik, K. V. Houcke, E. Gull, L. Pollet, N. Prokof'ev, B. Svistunov, and M. Troyer, "Diagrammatic monte carlo for correlated fermions," *EPL (Europhysics Letters)*, vol. 90, no. 1, p. 10 004, 2010.

[128] E. Burovski, N. Prokof'ev, and B. Svistunov, "Truncated-determinant diagrammatic monte carlo for fermions with contact interaction," *Phys. Rev. B*, vol. 70, p. 193 101, 2004.

[129] E. Burovski, N. Prokof'ev, B. Svistunov, and M. Troyer, "Critical temperature and thermodynamics of attractive fermions at unitarity," *Phys. Rev. Lett.*, vol. 96, p. 160 402, 2006.

[130] K. V. Houcke, F. Werner, E. Kozik, N. Prokof'ev, B. Svistunov, M. J. H. Ku, A. T. Sommer, L. W. Cheuk, A. Schirotzek, and M. W. Zwierlein, "Feynman diagrams versus fermi-gas feynman emulator," *Nature Physics*, vol. 8, no. 5, pp. 366–370, 2012.

[131] A. Fetter and J. Walecka, *Quantum Theory of Many-particle Systems*, ser. Dover Books on Physics. Dover Publications, 2003, ISBN: 9780486428277.

[132] I. V. Beloussov, "Another formulation of the wick's theorem. farewell, pairing?" *Special Matrices*, vol. 3, no. 1, 2015.

[133] N. Prokof'ev, private communications.

**Adriano ANGELONE**

# Strongly Correlated Systems of Bosons and Fermions: a Diagrammatic, Variational and Path Integral Monte Carlo study


## Résumé

Mon travail de thèse se concentre sur l'étude, à l'aide de techniques numériques, de systèmes de fermions et bosons fortement corrélés. J'étudie Hamiltoniens de bosons sur réseau avec interactions à portée étendue, avant un intérêt pour expériences concernant atomes en états Rydberg-dressed, par moyen de simulations Path Integral Monte Carlo. Mon résultat principal est la démonstration d'un état de superverre en absence de sources de frustration dans le système. J'étudie également la modèle t-J fermionique avec deux trous par moyen de simulations Variational Monte Carlo avec l'ansatz Entangled Plaquette States (EPS). Mon étude est fondamental en la perspective d'appliquer l'ansatz EPS à autres systèmes fermioniques, d'intérêt pour la supraconductivité à haute temperature, dont le comportement n'a pas encore été déterminé. Finalement, je présente mon travail sur une implémentation de l'algorithme Diagrammatic Monte Carlo.


**Mots-Clé**: *Physique de la Matière Condensée, Methodes Numériques, Simulation Quantique, Atomes de Rydberg, Path Integral Monte Carlo, Supersolide, Superglass, Supraconductivité à Haute Temperature, Modèle t-J, Variational Monte Carlo, Diagrammatic Monte Carlo.*


## Abstract

The focus of my thesis is the investigation, via numerical approaches, of strongly correlated models of bosons and fermions. I study bosonic lattice Hamiltonians with extended--range interactions, of interest for experiments with cold Rydberg-dressed atoms, via Path Integral Monte Carlo simulations. My main result is the demonstration of a superglass in the absence of frustration sources in the system. I also study the fermionic $t-J$ model in the presence of two holes via Variational Monte Carlo with the Entangled Plaquette States Ansatz. My study is foundational to the extension of this approach to other fermionic systems, of interest for high temperature superconductivity, where the physical picture is still under debate (such as, e.g., the $t-J$ model in the case of finite hole concentration). Finally, I discuss my work on an implementation of the Diagrammatic Monte Carlo algorithm.


**Keywords** : *Condensed Matter Physics, Numerical Methods, Quantum Simulation, Rydberg Atoms, Path Integral Monte Carlo, Supersolid, Superglass, High-Temperature Superconductivity, t-J Model, Variational Monte Carlo, Diagrammatic Monte Carlo.*